UNIVERSIDADE FEDERAL DO PARANÁ

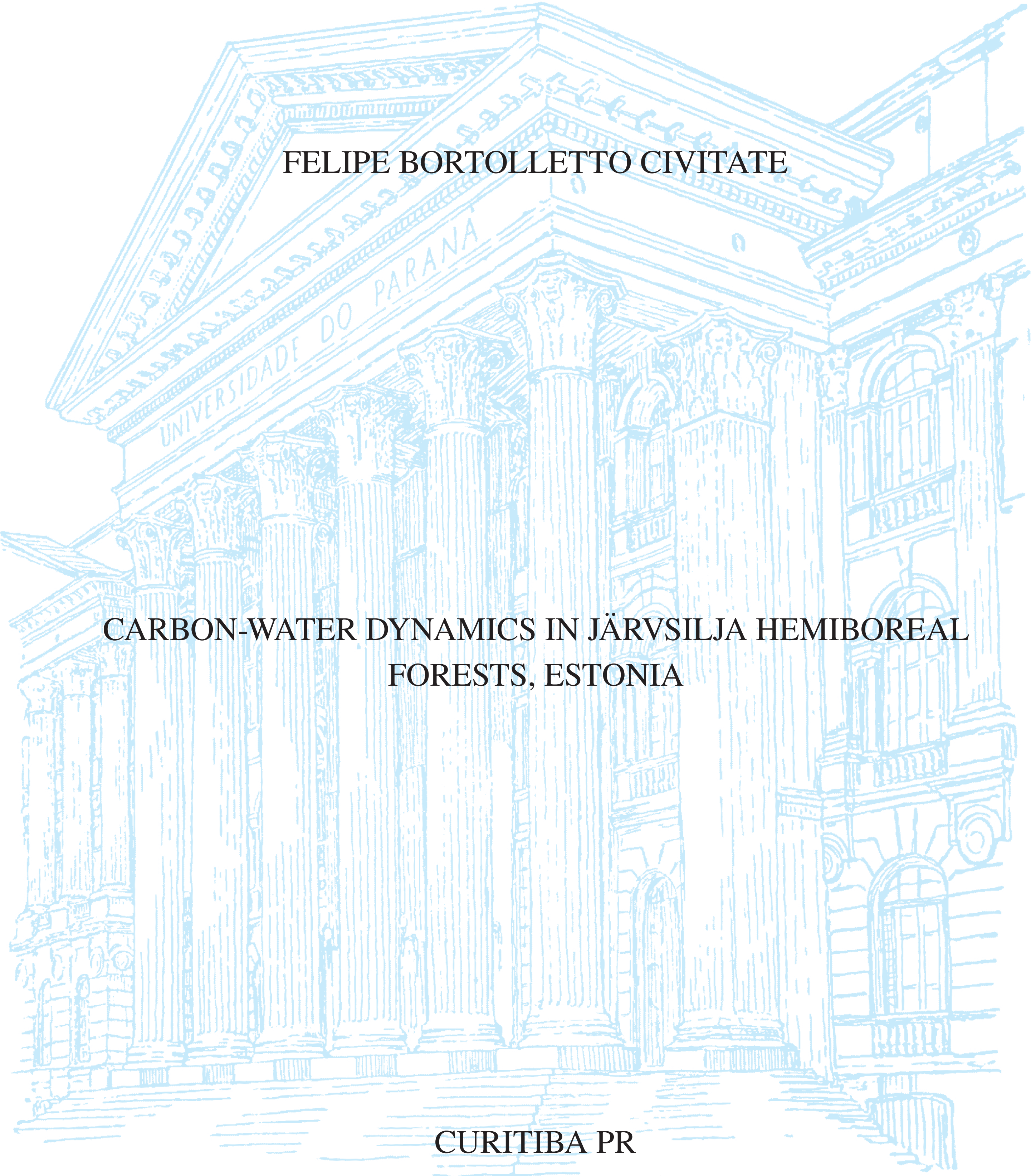

FELIPE BORTOLLETTO CIVITATE

CARBON-WATER DYNAMICS IN JÄRVSILJA HEMIBOREAL FORESTS, ESTONIA

CURITIBA PR
16 JANEIRO, 2026

FELIPE BORTOLLETTO CIVITATE

CARBON-WATER DYNAMICS IN JÄRVSILJA HEMIBOREAL FORESTS, ESTONIA

Dissertação apresentada como requisito parcial para a obtenção do título de Mestre em Engenharia Ambiental, no Programa de Pós-Graduação em Engenharia Ambiental (PPGEA), Setor de Tecnologia, Universidade Federal do Paraná..

Área de Concentração: *Tecnologia, observação e modelagem ambiental*.

Orientador: Emílio Graciliano Ferreira Mercuri.

CURITIBA PR
16 JANEIRO, 2026

DADOS INTERNACIONAIS DE CATALOGAÇÃO NA PUBLICAÇÃO (CIP)
UNIVERSIDADE FEDERAL DO PARANÁ
SISTEMA DE BIBLIOTECAS – BIBLIOTECA CIÊNCIA E TECNOLOGIA

Civitate, Felipe Bortolletto
Carbon–water dynamics in Järvselja hemiboreal forests, Estonia. / Felipe Bortolletto Civitate. – Curitiba, 2026.
1 recurso on-line : PDF.

Dissertação (Mestrado) - Universidade Federal do Paraná, Setor de Tecnologia, Programa de Pós-Graduação em Engenharia Ambiental.

Orientador: Emílio Graciliano Ferreira Mercuri

1. Carbono 2. Água.. 3. Floresta Hemiboreal 4. Ecossistemas - Estônia I. Universidade Federal do Paraná. II. Programa de Pós-Graduação em Engenharia Ambiental. III. Mercuri, Emílio Graciliano Ferreira. IV. Título.

Bibliotecária: Roseny Rivelini Morciani CRB-9/1585

MINISTÉRIO DA EDUCAÇÃO
SETOR DE TECNOLOGIA
UNIVERSIDADE FEDERAL DO PARANÁ
PRÓ-REITORIA DE PÓS-GRADUAÇÃO
PROGRAMA DE PÓS-GRADUAÇÃO ENGENHARIA AMBIENTAL - 40001016075P3

TERMO DE APROVAÇÃO

Os membros da Banca Examinadora designada pelo Colegiado do Programa de Pós-Graduação ENGENHARIA AMBIENTAL da Universidade Federal do Paraná foram convocados para realizar a arguição da Dissertação de Mestrado de **FELIPE BORTOLLETTO CIVITATE**, intitulada: **Carbon-Water Dynamics in Järvselja Hemiboreal Forests, Estonia**, sob orientação do Prof. Dr. EMILIO GRACILIANO FERREIRA MERCURI, que após terem inquirido o aluno e realizada a avaliação do trabalho, são de parecer pela sua APROVAÇÃO no rito de defesa.

A outorga do título de mestre está sujeita à homologação pelo colegiado, ao atendimento de todas as indicações e correções solicitadas pela banca e ao pleno atendimento das demandas regimentais do Programa de Pós-Graduação.

Curitiba, 09 de Fevereiro de 2026.

Assinatura Eletrônica
09/02/2026 17:45:47.0
EMILIO GRACILIANO FERREIRA MERCURI
Presidente da Banca Examinadora

Assinatura Eletrônica
09/02/2026 20:05:48.0
MAURÍCIO FELGA GOBBI
Avaliador Interno (UNIVERSIDADE FEDERAL DO PARANÁ)

Assinatura Eletrônica
10/02/2026 08:19:06.0
STEFFEN MANFRED NOE
Avaliador Externo (ESTONIAN UNIVERSITY OF LIFE SCIENCES)

Ao movimento, à mudança, à terra e aos seus ciclos. A tudo que a vida toca em seu eterno movimento.

Acknowledgments

I am immensely grateful for the two years of learning, development, and opportunities I have been granted. It has been a period of intense study, dedication, and constant improvement. UFPR proves to be an institution of excellence, fostering both scientific advancement and the growth of individuals capable of building a better society, while strengthening the connection between citizens and the environment they inhabit.

None of this would have been possible without the support of my professors, who guide and mentor me, providing the foundation for me to walk with confidence through the unknown. I offer special thanks to Professor Emilio Mercuri, who, beyond being my advisor, has become a friend for whom I hold eternal affection and loyalty, as a result of all the guidance and support provided over these past two years.

I would also like to thank the Estonian University of Life Sciences (EMÜ) and Professor Steffen Noe for providing not only the data necessary for this research but also for opening my eyes to a new culture and a new way of perceiving life and the ecosystem.

This study was financed in part by the Coordenação de Aperfeiçoamento de Pessoal de Nível Superior - Brasil (CAPES) - Finance Code 001.

RESUMO

Este trabalho investiga a dinâmica de carbono e água em florestas hemiboreais, com foco na região de Järvselja, Estônia, e especificamente na bacia hidrográfica florestada de Kalli. O objetivo principal foi analisar e quantificar elementos dos ciclos hídrico e de carbono, avaliando a interação entre a disponibilidade de água no solo e a Troca Líquida do Ecossistema (NEE). Para isso, foram empregadas três abordagens de modelagem hidrológica: o modelo conceitual GR4J-Cemaneige, um modelo de aprendizado de máquina baseado em Redes Neurais Recorrentes (Memória de Longo e Curto Prazo - LSTM) e uma arquitetura híbrida que integra variáveis de estado físicas à rede neural. Uma técnica de diagnóstico (denominada sonda, baseada em Regressão de Vetores de Suporte) foi utilizada para avaliar a capacidade do modelo de representar fisicamente a umidade do solo a partir de seus estados internos. Dados de fluxos de carbono, derivados de medições por covariância de fluxos turbulentos e processados pelo programa REddyProc, foram analisados em conjunto com o balanço hídrico da bacia em escalas temporais diária, mensal e anual.Os resultados na bacia de Reola indicaram que o modelo híbrido apresentou o melhor desempenho estatístico ($NSE = 0,887$), superando tanto o modelo de aprendizado de máquina isolado ($NSE = 0,827$) quanto o modelo conceitual puro ($NSE = 0,503$). A sonda de umidade do solo demonstrou alta capacidade de capturar a dinâmica temporal da variável, com excelentes correlações nas camadas intermediárias do solo. A análise dos fluxos confirmou o comportamento sazonal esperado, com a floresta atuando como consumidor de carbono na primavera e verão e como fonte ou neutra no outono e inverno. Identificou-se uma tendência de redução no sequestro de carbono associada à diminuição da disponibilidade hídrica ao longo do período de estudos. Esse acoplamento foi evidenciado pela onda de calor de 2018, que provocou a estagnação da função de sumidouro do ecossistema e revelou um efeito de memória na recuperação da vegetação nos anos subsequentes. Conclui-se que a combinação de modelagem híbrida e análise de fluxos permitem uma melhor compreensão das interações ecossistêmicas, destacando a sensibilidade do balanço de carbono em relação à disponibilidade hídrica terrestre em florestas hemiboreais.

Palavras-chave: Dinâmica Carbono-Água, Floresta Hemiboreal, Modelagem Hidrológica,Troca Líquida do Ecossistema (NEE), Estônia.

ABSTRACT

This study investigates carbon and water dynamics in hemiboreal forests, focusing on the Järvselja region, Estonia, and specifically the Kalli forested catchment. The main objective was to analyze and quantify the water and carbon cycles, assessing the interaction between soil water availability and Net Ecosystem Exchange (NEE). For this purpose, hydrological modeling approaches were employed, including the conceptual GR4J-Cemaneige model, a standalone Long Short-Term Memory (LSTM) machine learning model, and a hybrid LSTM+GR4J architecture. A diagnostic technique (Support Vector Regression-based probe) was used to evaluate the LSTM's ability to physically represent soil moisture from its internal cell states. Carbon flux data, derived from eddy covariance measurements, were analyzed in conjunction with the catchment water balance on daily, monthly, and annual time scales. Results for the Reola basin indicated that the hybrid model achieved the best performance ($NSE = 0.887$), surpassing the standalone LSTM ($NSE = 0.827$) and the GR4J model ($NSE = 0.503$). The soil moisture probe was able to capture the variable's temporal dynamics, with correlations reaching $r = 0.99$ for intermediate root zones. NEE analysis confirmed the expected seasonal behavior, where the forest acts as a carbon sink in spring and summer and as a source or neutral in autumn and winter. An increasing trend in NEE (reduced sequestration) was identified in association with a decreasing trend in water availability, most notably during the 2018 heatwave, which caused the stagnation of the ecosystem's sink function. It is concluded that the combination of hybrid modeling and carbon flux analysis allows for a better understanding of ecosystem interactions and sensitivity to drought conditions.

Keywords: Carbon-Water Dynamics, Hemiboreal Forest, Hydrological Modeling, Net Ecosystem Exchange (NEE),Estonia.

List of Figures

List of Tables

List of Acronyms

ANN	Artificial Neural Network
BIAS	Bias (Mean Bias Error)
CAMS	Copernicus Atmosphere Monitoring Service
CAMELS	Catchment Attributes and Meteorology for Large-Sample Studies
Cemaneige	Centre d'Études des Neiges Snow Model
CNN	Convolutional Neural Network
DDS	Dynamically Dimensioned Search
DG AGRI	European Commission, Directorate-General for Agriculture and Rural Development
EC	Eddy Covariance
ECMWF	European Centre for Medium-Range Weather Forecasts
ERA5	Fifth Generation ECMWF Atmospheric Reanalysis of the Global Climate
ESA	European Space Agency
EEO	Estonian Environmental Observatory
ET	Evapotranspiration
FFP	Flux Footprint Prediction
GPP	Gross Primary Production
GR4J	Génie Rural à 4 paramètres Journalier
GRU	Gated Recurrent Unit
IPCC	Intergovernmental Panel on Climate Change
KGE	Kling–Gupta Efficiency
LSTM	Long Short-Term Memory
MAE	Mean Absolute Error
MODIS	Moderate Resolution Imaging Spectroradiometer
MSE	Mean Squared Error
NASA	National Aeronautics and Space Administration
NEE	Net Ecosystem Exchange
NEP	Net Ecosystem Production
NLP	Natural Language Processing
NOAA	National Oceanic and Atmospheric Administration
P	Precipitation
PINN	Physics-Informed Neural Network
PPGEA	Programa de Pós-Graduação em Engenharia Ambiental
Q	Discharge (Streamflow)
Reco	Ecosystem Respiration
RMSE	Root Mean Square Error
r	Pearson Correlation Coefficient

SCT1	Scaffold Tower One
SCT2	Scaffold Tower Two
SMAP	Soil Moisture Active Passive
SMEAR	Station for Measuring Forest Ecosystem–Atmosphere Relations
SVM	Support Vector Machine
SVR	Support Vector Regression
UH	Unit Hydrograph
UFPR	Universidade Federal do Paraná
VPD	Vapor Pressure Deficit

SUMÁRIO

Chapter 1

Introduction

The global carbon cycle involves continuous exchange of carbon among the atmosphere, oceans, and terrestrial biosphere, driven by physical, chemical, and biological processes (Friedlingstein, 2023). Oceans serve as major carbon sinks, while forests regulate atmospheric CO_2 through photosynthesis, respiration, and decomposition. Human activities — particularly fossil fuel combustion and land-use changes — have disrupted this natural balance, significantly increasing atmospheric CO_2 concentrations (Evans, 2016). These emissions have led to a consistent annual rise in CO_2 levels, with NOAA (National Oceanic and Atmospheric Administration) reporting a global average of 426 ppm in February 2024, over 50% higher than pre-industrial levels (NOAA , 2024).The Intergovernmental Panel on Climate Change (IPCC) socioeconomic pathways project potential temperature increases ranging from 1.5°C to 5.7°C (Meinshausen, 2020).

Accurate estimation of forest ecosystem carbon and water fluxes are crucial for addressing global environmental change (Dou and Yang, 2017). The Net Ecosystem Production (NEP) represents the net carbon balance of an ecosystem, indicating carbon accumulation. Essentially, NEP is the negative of Net Ecosystem Exchange (NEE) ($NEP = -NEE$). NEE represents the net exchange of CO_2 between the ecosystem and the atmosphere (Waring and Running, 1998). It's calculated as the difference between Gross Primary Production (GPP), which is the carbon fixed through photosynthesis, and total Ecosystem Respiration (R_{eco}). The equation for NEE is:

$$NEE = GPP - R_{\text{eco}}$$

Using the eddy covariance approach and the IPCC B2 scenario (+3.1°C, -27% summer precipitation), Davi et al. (2006) projected a median 40% increase in GPP and a 31% increase in R_{eco} across various European ecosystems from 1960 to 2100. While initially appearing to enhance forest carbon sequestration ($NEP = GPP - R_{eco}$), species- and climate-specific responses to water stress reveal a more nuanced picture: conifers became carbon sinks, while evergreen deciduous trees exhibited increased emissions.

Elevated atmospheric CO_2 can enhance photosynthesis and gross primary productivity (GPP) in forests (Sperry et al., 2019). While forests may acclimatize to rising temperatures, mitigating warming's negative impacts and amplifying CO_2 gains, this benefit depends on CO_2 and temperature remaining within a critical threshold. Exceeding this threshold leads to increased vapor pressure, exacerbating water stress in trees, inducing stomatal closure, drying soils, and ultimately causing mortality via vascular cavitation.

The importance of water and carbon dynamics is evident. In snowy regions, the absence of soil moisture data during periods of water accumulation in a solid state severely impacts the reproduction of hydrological systems and the closure of the hydrological balance, as demonstrated by Pan et al. (2017). Understanding the system requires accounting for factors such as moisture redistribution, snow accumulation, seasonal melting, and subsurface interactions. For instance, subsurface exchanges in hydrological microbasins can represent up to 25% of the regional water balance (Safeeq et al., 2021). These hydrological processes are closely connected to carbon dynamics, Ishizuka et al. (2006) investigated the relationship between soil temperature and CO_2 fluxes across 26 Japanese forests, finding that colder regions have a greater potential for increased carbon fluxes, with water balance playing a critical role in modulating the sensitivity of CO_2 emissions to temperature. Further illustrating the interplay between water and carbon fluxes, a study conducted in subtropical mangroves in southern China (Gou et al., 2023) found that these ecosystems act as highly efficient, seasonally dependent carbon sinks, strongly influenced by multifactorial flooding conditions.

The complexity of environmental phenomena is not new, and for this very reason, machine learning techniques have emerged as valuable tools in the environmental sciences (Mohan et al., 2025). For hydrological studies, these methods are used to model different processes of the water cycle (Mohammadi, 2021), often performing better than conventional models and in situations of uncertainty or data absence. Studies indicate that these methods are capable of capturing complex nonlinear relationships between carbon fluxes and environmental drivers (Ezhova et al., 2025; Dou et al., 2018; Dou and Yang, 2017).

Another great ally of environmental studies is data from remote sensing, constituting a tool for obtaining data on a large temporal and spatial scale (Khanbilvardi et al., 2014). Different sources are used for monitoring soil cover data, biomass estimates, temperature estimates, radiation, surface soil moisture and other meteorological variables (Kazemi Garajeh et al., 2024). The combination of data from different sensors, as well as the implementation of correction and modeling methodologies based on data measured in the field, enables a more complete view of environmental phenomena (Quiroz Jiménez and Collischonn, 2015).

Extreme weather events are indicative of the impact of rising average temperatures (Krasnova et al., 2022). In Europe, the intense heat wave of 2018 illustrates this effect, characterized by exceptionally hot and dry conditions during the summer and spring, causing high temperatures, intense radiation, and severe water deficit, anticipating the water stress of the flora (Bastos et al., 2020). Occurring with greater severity in typically cold and humid countries in northern and central Europe, Peters et al. (2020) discuss that in many regions photosynthesis (GPP) was drastically reduced, while respiration varied, resulting in a drop in net carbon sequestration (NEP). Still, in some areas—especially in southern Europe—the warm, wet spring allowed for above-average harvests before the peak of the drought.

This work is situated within this context, seeking to advance the understanding of water-carbon dynamics in hemiboreal forests, with a focus on the Järvselja region, Estonia. The differential scientific contribution of this research lies in the combination of multiple methodological approaches for an integrated analysis. Specifically, this study performs a direct comparison and performance evaluation between a conceptual hydrological model (GR4J-Cemaneige) and a machine learning model (LSTM) for streamflow simulation, including its regionalized application in an ungauged basin (Kalli). Additionally, an interpretability technique is employed to extract and validate physical representations (soil moisture) of the internal states of the LSTM model, addressing the challenge of interpretability of ML models in hydrology. Connecting hydrological simulations and the derived water balance with observed data of Net Ecosystem Exchange (NEE) at multiple temporal scales, quantifying the water-carbon coupling and evaluating the impact of extreme climatic events, such as the 2018 heatwave, on this specific ecosystem.

We aim to investigate the carbon–water dynamics within the Kalli Basin by integrating hydrological modeling with eddy covariance data. Our focus is to assess the impacts of climate change on regional climate conditions, soil moisture, and the forest's carbon sequestration potential. This research seeks to determine the feasibility of using observational data and model simulations to quantify the effects of climate change and extreme weather events. The 2018 heatwave will serve as a case study to analyze the forest's response and recovery mechanisms. A key objective is to develop a robust methodology for simulating streamflow in the Reola Basin by combining the GR4J-Cemaneige model with a physics-informed LSTM (Long Short-Term Memory) neural network. Additionally, we aim to enhance our understanding of LSTM model behavior by employing diagnostic tools to investigate whether it can learn and represent physical processes, such as soil moisture dynamics.

Chapter 2

Literature Review

In this chapter, we present a review of the main concepts, methodologies, and advances related to hydrological modeling and net ecosystem exchange in ecosystems. We begin by addressing modeling techniques based on recurrent neural networks, focusing on machine learning applications in hydrology, highlighting traditional conceptual models and recent data-driven approaches. Next, we discuss the concept and applications of Net Ecosystem Exchange (NEE), detailing its importance for understanding the carbon balance and its relationship with environmental variables, highlighting its significance as a measure of ecosystem carbon balance and its response to climatic changes.

2.1 Recurrent Neural Networks for hydrological modelling

Machine Learning (ML) refers to a set of techniques and algorithms that enable prediction systems to learn from data, improving their performance without being explicitly programmed. The main objective is to develop equations that, once trained, can represent natural phenomena based on observed patterns in data rather than on physical principles (Zhou (2021)). ML is generally divided into two main categories: supervised learning, which relies on labeled input-output pairs to guide the training process, and unsupervised learning, which seeks to uncover hidden patterns in data without predefined labels (Babovic, 2009; Zhou, 2021).

The application of ML in environmental sciences has grown significantly in recent years, driven by technological advancements and the increasing availability of large datasets (Razavi et al., 2022; Xu and Liang, 2021). ML has proven to be a promising approach, particularly when combined with traditional physics-based hydrological models, as it offers new possibilities for modeling and predicting complex environmental phenomena Ghobadi and Kang (2023). Among the most widely used algorithms are artificial neural networks (ANNs), which offer benefits such as adaptive learning capacity, error tolerance, and distributed processing—despite challenges such as selecting optimal architectures and dealing with unpredictable network behavior (Saha and Pal, 2024).

Support Vector Regression (SVR) is another popular ML technique grounded in statistical learning theory and the principles of Support Vector Machines (SVM). The central goal of SVR is to find a regression function that generalizes well to unseen data by minimizing the generalization error (Vapnik, 1998). Unlike other regression models, SVR employs the principle of structural risk minimization (SRM), which aims to minimize an upper bound on the generalization error, rather than just minimizing the training error. This results in a better generalization capability for new data (Acosta, 2019).

The hydrological literature presents a variety of approaches for transforming hydrologic inputs into outputs, traditionally categorized into physical, systems (or empirical), and conceptual models (Cantoni et al., 2022). The physical approach relies on fundamental conservation laws of fluid mechanics and thermodynamics to describe the movement of water within the hydrologic cycle, but its application is often limited by the complexity and variability of natural catchments and the difficulty in defining accurate boundary conditions. In contrast, the systems or empirical approach treats the hydrologic system as a "black box," focusing on statistical or functional relationships between inputs and outputs without explicit consideration of internal physical processes. Recognizing that many methods fall between these extremes, the implementation of "grey boxes" has emerged—representing key hydrologic processes through response functions inspired by physically meaningful but tractable formulations. Despite this classification, distinctions among these paradigms often blur in practice, as what constitutes a physical model in one context may represent an empirical simplification in another (Brutsaert, 2005).

Illustrating this, the GR4J (Génie Rural à 4 paramètres Journalier) model represents one of these middle-ground approaches. It was developed by the French National Institute for Agricultural Research, Food, and Environment (Perrin et al., 2003) and is a conceptual model designed to simulate surface runoff. With only two input variables—daily precipitation and potential evapotranspiration—it captures the physical context of the hydrological system while providing a practical representation that is not strictly constrained by fundamental conservation laws. Furthermore, snow accumulation and melting within a watershed can be simulated through the CemaNeige model, developed by (Valéry, 2010), which has been integrated into GR4J. By using minimum and maximum air temperatures together with altitude data, CemaNeige estimates snow storage and melting dynamics, contributing to runoff generation. Several studies have assessed the accuracy of GR4J, using it to validate global reanalysis precipitation data (Gu, 2023; Andrade et al., 2024; Nemri and Kinnard, 2020), as well as to evaluate its performance in operational forecasting systems (Wijayarathne and Coulibaly, 2020) and regionalization methodologies (Karki, 2023; Kuana et al., 2024; Nemri and Kinnard, 2020)

While conceptual models like GR4J aim to balance physical realism with practical simplicity, recent advances have increasingly turned towards data-driven approaches. These methods, including machine learning techniques (ML), seek to capture complex input-output relationships directly from observed data, often without relying on explicit representations of physical processes. Among these, Recurrent Neural Networks (RNNs) are architectures designed to handle sequential data, as they can retain information from previous inputs that influences future predictions (Karpathy, 2015). A particular type of RNN, the Long Short-Term Memory (LSTM) network, was proposed by Hochreiter and Schmidhuber (1997) to overcome limitations of standard RNNs by incorporating mechanisms that allow the model to selectively retain or discard information over long sequences, improving its ability to model temporal dependencies.

LSTM has been frequently studied for hydrological applications. Kratzert et al. (2018) conducted different types of tests on 241 basins in the United States, and it was possible to discover that LSTM is capable of predicting runoff from meteorological observations, with few data requirements and accuracies comparable to well-established physical models. Using only two inputs, temperature and precipitation. Similarly, Sabzipour et al. (2023) applied an LSTM model to forecast streamflow in a Canadian catchment and compared its performance with a process-based distributed hydrological model Sacramento Soil Moisture Accounting (SAC-SMA) driven by the same meteorological forecasts.

Zhang et al. (2018) developed an enhanced LSTM-based model for predicting water table depth in agricultural regions, incorporating a fully connected layer and dropout to improve performance and prevent overfitting, thereby creating a novel forecasting approach. Similarly, Sahoo et al. (2019) found that LSTM outperformed both RNN and naive forecasting methods in modeling low-flow hydrological time series, attributing this success to LSTM's superior ability to remember and update information. Conversely, Frame and Kratzert (2022) achieved an outperforming peak flow prediction with data-driven models when comparing with benchmark physical models; even a hybrid physical-LSTM model approach performed worse than a purely data-driven LSTM in the study. Graves and Schmidhuber (2005) investigated LSTM capabilities for water quality parameters, including Bi-LSTM variants, which accelerate learning by processing data in both forward and reverse time directions. Hybrid models such as CNN-LSTM and CNN-GRU combine the feature extraction capabilities of CNNs with the temporal forecasting of LSTMs and GRUs, showing higher stability in handling data with large fluctuations (Wai et al., 2022).

Kratzert et al. (2019a) uses LSTM neural networks to handle multiple basins, in contrast to traditional hydrological models that often underperform when calibrated for a specific region, composed of similar basins. The version proposed by the author, Entity-Aware LSTM (EA-LSTM), is characterized by learning the hydrological system in the region based on the physical attributes of each basin, in addition to the meteorological data. When applying this model to 531 North American basins, results were superior to the reference physical models, both for models calibrated for individual basins and for regionalized models. Arsenault et al. (2023) investigates the application of LSTM for flow prediction in ungauged basins, analyzing 150 North American basins. The author's results outperformed conventional models, especially in scenarios with a lack of input data.

Recent research investigates bridging data-driven models with physical representations. For instance, Lees et al. (2022) showed that LSTMs, during training, implicitly learn meteorologically relevant features, with internal states resembling soil moisture and snowpack. This suggests LSTMs can produce accurate discharge predictions underpinned by physical consistency. By probing internal state vectors with a linear probe (using meteorological and static inputs, but without explicit snow cover or soil moisture data), they found strong correlations (≥ 0.8) between LSTM states and ERA5 soil moisture reanalysis data, highlighting the technique's potential for interpreting the physical relevance of LSTM outputs. In a related effort, Raissi et al. (2024) explored a hybrid approach using Physics-Informed Neural Networks (PINNs)—universal function approximators that integrate physical principles to solve PDE-governed datasets—thus grounding ANN learning in physical laws.

2.2 Net Ecosystem Exchange (NEE)

The Net Ecosystem Exchange (NEE) is a quantitative and direct measure of the net carbon exchange between the ecosystem and the atmosphere. It represents the balance between carbon uptake through photosynthesis (Gross Primary Production, GPP) and carbon release through ecosystem respiration (R_{eco}), the plants and the soils. It is a measure that can help us to identify if the ecosystem is a carbon sink or a source, being affected by radiation, air temperature, the water vapor pressure deficit (VPD), while the Respiration is influenced by air and soil temperature, soil content, the quantity and quality of organic matter, nutrient availability, as well as the Carbon supply to roots (Krasnova, 2019; Chapin et al., 2006)

The conceptual framework of NEE can be expressed through the equation 2.1, if the values of NEE are negative, the environment related to that is a carbon sink, and a carbon source if NEE are positive.

$$\mathrm{NEE} = R_{\mathrm{eco}} - \mathrm{GPP} \tag{2.1}$$

Respiration (R_{eco}) and Gross Primary Production (GPP) are strongly conditioned by seasonal temperature variations. During the colder months, in winter, both photosynthetic activity and respiration are reduced due to low temperatures and limited light availability. As temperatures rise in spring, there is a direct stimulus to photosynthesis and the biological activity of soil and vegetation, simultaneously increasing GPP and R_{eco} values. In summer, with ideal temperature and solar radiation conditions, GPP reaches its peak, reflecting the height of photosynthetic activity, while respiration also intensifies due to the increased metabolism of plants and microorganisms. In autumn, the gradual decrease in temperature leads to vegetation senescence, reducing both photosynthesis and respiration. Thus, temperature acts as one of the main seasonal regulators of these two carbon fluxes, determining the intensity of CO_2 exchange between the ecosystem and the atmosphere throughout the year.

Cellular respiration breaks down complex organic compounds, such as carbohydrates and fats, to produce energy, CO_2, and consume oxygen (Reichle, 2020). In contrast, photosynthesis, performed by autotrophic organisms such as plants, converts light energy into chemical energy, consuming CO_2 and water and releasing O_2, in addition to storing carbon in the form of tissues and sugars (Kluge et al., 2015). Notably, water is consumed in photosynthesis and produced in cellular respiration, making it a limiting factor for photosynthesis. Mendes et al. (2020) analyzed the Caatinga, a seasonally dry tropical forest in Brazil, during the 2014-2015 drought using NEE data and its relationship with precipitation, radiation, and temperature. The results indicated an annual accumulation of 160 gCm^2, suggesting that the biome functioned as a carbon sink during the dry season, maintaining sufficient water levels for photosynthesis even without precipitation. In contrast, Hayek et al. (2018) demonstrated, by empirically modeling NEE in the Amazon for 10 years, that prolonged droughts drastically reduce the photosynthetic capacity of the vegetation.

A Danish study by Pilegaard and Ibrom (2020) analyzed 23 years of data in *Fagus sylvatica* forests and demonstrated that these ecosystems consistently acted as carbon sinks, with an average increase in carbon uptake of approximately $15\,\mathrm{g\,C\,m^{-2}\,yr^{-1}}$, primarily driven by regional warming and the resulting extension of the growing season. However, interannual variability in carbon dynamics was strongly influenced by climate extremes. The severe European drought of 2018, for instance, reduced NEE by about 25%, mainly due to a sharp decline in GPP, while RE remained low, partially offsetting the effect on NEE. The annual carbon uptake in 2018 was approximately 100 g C lower than expected based on the historical trend. Other years, such as 2008, also showed reduced summer carbon assimilation. In addition to climate impacts, structural disturbances such as forest thinning also play a significant role: Lindroth et al. (2018) reported a 30% reduction in daytime assimilation following a 25% reduction in forest volume, with NEE returning to pre-disturbance levels only after eight years.

The Järvselja forest and the SMEAR station (Station for Measuring Ecosystem-Atmosphere Relations) have already been the subject of other studies. Krasnova (2019) performed continuous CO_2 measurements, evaluating carbon fluxes in different forest compositions in the region, and found that, in 2015, the forest acted as a carbon sink, with NEE close to -600 gC m-2 yr-1, exceeding the typical values of pure boreal forests. Subsequently, Krasnova et al. (2022) investigated carbon flux in new distinct forest compositions on the same region during the 2018 heatwave. Mercuri et al. (2023), while studying the water balance and carbon fluxes in the region, found evidence that the system is becoming a progressively weaker carbon sink. The average NEE increased from $-1.23\ \mu\mathrm{mol\ m^{-2}\ s^{-1}}$ in 2015 to $-0.62\ \mu\mathrm{mol\ m^{-2}\ s^{-1}}$ in 2020. As a consequence, water availability ($\Delta s = P - ET - Q$) declined from 0.24 mm to -0.05 mm over the same period.

Chapter 3

Materials and methods

This chapter aims to describe in detail the study area, the datasets, and the methodological procedures used in the present work. It begins with a characterization of the geographical and climatic context of southeastern Estonia, focusing on the Reola and Kalli basins and the SMEAR Estonia station. Then, the main data sources, including meteorological, hydrological, and remote sensing products, are presented. Finally, this chapter describes the data analysis and models applied to the datasets, illustrated in the diagram shown in Figure 3.1, providing the steps and expected results.

Figure 3.1 is divided into two parts. The upper part illustrates the procedures for the hydrological simulation of the Reola (green) and Kalli (yellow) basins (Section 3.1). The input variables are shown in purple, including meteorological data from the Tartu and Võru stations and georeferenced data from MODIS. The calibration was first performed for Reola using the GR4J model (Section 3.2.5), and its parameters were subsequently adapted for the LSTM model (Section 3.2.2). With both models calibrated, their parameters were regionalized (Section 3.2) to the Kalli basin, generating simulated streamflow series. The internal probe applied to the LSTM (Section 3.2.3) was also analyzed. The lower part of the figure shows, once again in purple, the input data from the SMEAR station (Section 3.1) and the georeferenced data (Section 3.6) used to generate the NEE, GPP, and RE_{eco} series (Section 2.2), with the methodology highlighted in pink.

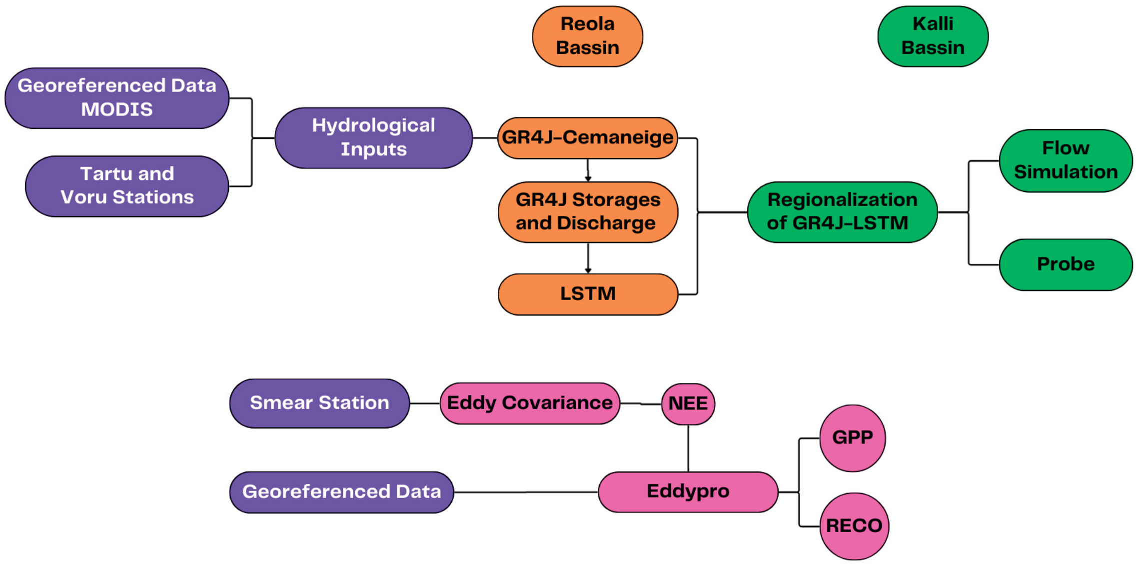

Figure 3.1: Overview of the hydrological and carbon flux modeling procedures. The upper part illustrates the calibration and regionalization steps for the Reola (orange) and Kalli (green) basins, including the input variables (purple) from meteorological stations (Tartu and Võru) and MODIS georeferenced data. The GR4J model was first calibrated for Reola, with its parameters adapted for the LSTM model. Both models were then regionalized to the Kalli basin to generate simulated streamflow, and a probe (SVR) was applied internally to the LSTM. The lower part shows the input data (purple) from the SMEAR station and georeferenced sources used to generate NEE, GPP, and RE_{eco} series, with the methodology highlighted in orange.

3.1 Study Area

Figure 3.2(b) illustrates the north-eastern part of Europe, specifically Estonia, a northern European country that borders the guld of Finland to the north, Russia to the east, and Latvia to the south, and is bathed by the Baltic Sea. An European Union member since 2004, Estonia has an area of 45.336 (European Union, 2025). Approximately 82% of Estonian territory is classified as rural area, where 44.5% of the population resides. Estonia has 11,300 farms, and approximately half of its rural area is covered by forests,which represent 50% of the national territory (DG AGRI, 2020). Agricultural land accounts for 25% of Estonian territory. Data from the Food and Agriculture Organization of the United Nations (FAO) show an increase in forest area and forest carbon stock in Estonia between 1990 and 2020. Approximately 9% of regenerated and planted forests are from natural regeneration and 22% of Estonian forests are located in protected areas (FAO, 2020).

Estonian forests are highly valued, driven by economic, social, ecological, and cultural motivations for their maintenance and preservation. Economically, approximately 72% of these forests are primarily designated for commercial use, supporting around 35.000 jobs in the forestry sector alone, with additional employment generated through tourism, sports, and hunting (European Commission, 2020). Beyond their economic and social such as recreation and emplyment, forests are crucial for the preservation of species diversity and for maintaining ecosystem health and environmental vitality. Furthermore, forests are deeply ingrained in

Estonian culture, forming an intrinsic part of the nation's identity (Estonian Ministry of Climate, 2024; Estonian Ministry of Environment, 2013).

Our study area, encompasses the Reola and Kalli watersheds, both draining into the Emajõgi River, which flows into Lake Peipsi. The Reola and Kalli Rivers are the primary tributaries of their respective basins. Figure 3.2(a) illustrates the detailed configuration of the study area, showing the Reola hydrometric station and two meteorological stations (Tartu–Tõravere and Võru) that provide long-term precipitation and temperature records. Also marked is the SMEAR Estonia station located within the Kalli basin, along with the Järvselja forest area. Different symbols indicate the type of station: hydrometric, meteorological, or ecosystem-atmosphere measurement. The broader context is shown in Figure 3.2(b), situating the study area within the Baltic region. The rectangle marks the location of the detailed map.

Although both Reola and Kalli represent relatively small catchments, with areas of $236.4\,\mathrm{km}^2$ and $55.6\,\mathrm{km}^2$ respectively, the use of daily temporal resolution for hydrological analysis remains appropriate due to the distinct geomorphological context of Estonia. The country is characterized by a flat topography, with low relief and gentle slopes dominating the landscape. As a result, water movement across the surface and subsurface tends to be slow, and travel times within the catchments are typically longer than in steep mountainous regions. Previous field observations and hydraulic analyses indicate that runoff propagation in both watersheds occurs gradually, with limited flashiness or rapid drainage, thus supporting the validity of daily aggregation for capturing hydrological processes.

Historically a poorly drained lowland, the area was subject to anthropogenic drainage through the construction of ditches to convert wetlands into managed forest. While these artificial drainage structures were designed to facilitate surface runoff, their capacity to accelerate the basin-scale hydrological response is heavily buffered by two main physical factors. First, the extremely flat topography and shallow gradients of the region mean that water velocities even within the ditches remain low. Second, the highly porous nature of the forested soils—particularly those rich in organic matter from previous wetland conditions—acts as a hydrological sponge. This high infiltration and water retention capacity ensures that precipitation is absorbed and released slowly into the drainage network as subsurface flow, preventing rapid overland runoff. Consequently, the time of concentration for the basin is prolonged, and the overall hydrological response remains sufficiently attenuated to fully justify the use of a daily time step in both modeling and observational comparisons.

The watersheds were delineated using a 25-meter resolution digital elevation model from the Estonian Topographic Database. Land cover classification, derived from the 2017 European Spatial Agency (ESA) data with 10m resolution, reveals contrasting land use patterns. The Kalli basin ($55.6\,\mathrm{km}^2$) is heavily forested (74.9%), with rangelands covering 24.6% and other land uses comprising only 0.5%. No agricultural areas were recorded. In contrast, the Reola watershed ($236.4\,\mathrm{km}^2$) is also predominantly forested (54.8%), but includes significant agricultural land (30.3%) and pastures/other vegetation (14.9%).

The Järvselja area is composed of 62.7% forest and 30.2% wetlands. Officially opened on August 23, 2015, the station is part of the "Estonian Research Infrastructures Roadmap" project (Estonian Environmental Observatory) and focuses on atmosphere-biosphere interactions, marine and limnological sciences, and land ecosystems research and monitoring (SMEAR Estonia, 2025).

The SMEAR Estonia (Station for Measuring Ecosystem-Atmosphere Relations) (58.27° N, 27.27° E, 36m altitude) at the Järvselja Experimental Forestry station measures energy and matter fluxes and concentrations in a hemiboreal forest (SMEAR Estonia, 2025). Adapted from the original SMEAR concept, originated in Finland (Hari et al., 2013), it is designed to conduct a

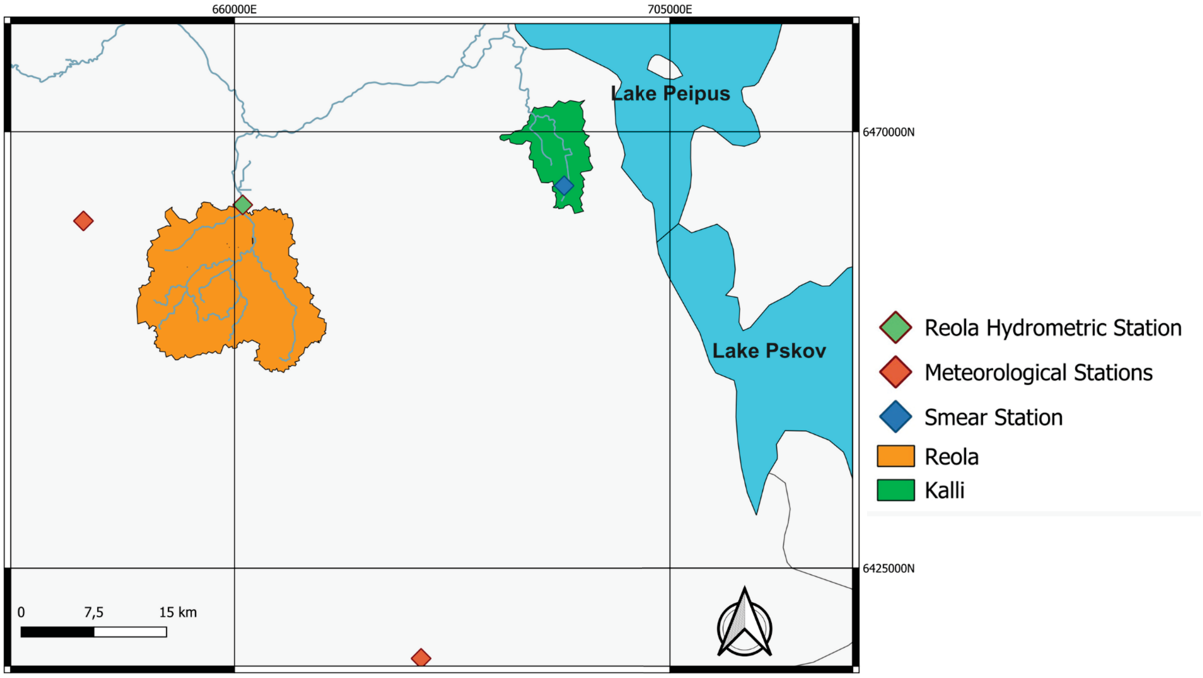

(a) Study area showing the Reola and Kalli watersheds, the Reola hydrometric station, meteorological stations (Tartu–Tõravere and Võru), and the SMEAR Estonia station. Main rivers are highlighted: Emajõgi River (gray line), which drains both basins into Lake Peipsi, and the Reola and Kalli rivers.

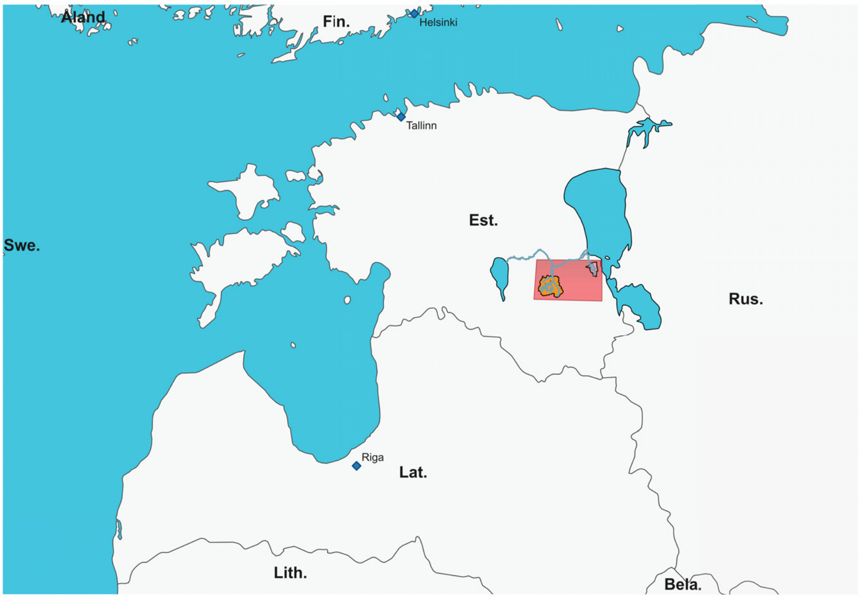

(b) Location of the study area in southeastern Estonia, near the border with Russia. The highlighted rectangle indicates the extent of the detailed map in Figure 3.2(a).

Figure 3.2: Location and characteristics of the study area. The Reola and Kalli basins, as well as key monitoring stations, are indicated. The Emajõgi River drains both basins into Lake Peipsi. Different symbols distinguish hydrometric, meteorological, and ecosystem-atmosphere measurement stations.

comprehensive suite of continuous, long-term measurements targeting two major categories: i) atmospheric composition and aerosols and ii) forest ecosystem and meteorological fluxes. To account for the higher tree species diversity and heterogeneity of this hemiboreal mixed forest region when compared with boreal forests, the measurement approach incorporates an additional canopy layer, reflecting the greater complexity of these ecosystems (Noe and Niinemets, 2015).

The station features a 130 m atmospheric measurement tower, a main cottage housing essential infrastructure (power supply, backup systems, internet, gas pumpers), an aerosol cottage, two 30 m scaffolding towers, and a container measurement site. A separate 24 m scaffolding tower (Liispõllu), with a shelter and power supply, is located 3 km west of the main station.

Measurements include 3D turbulent wind flow (Metek uSonic-3 Class A, 10 Hz), enabling net ecosystem exchange estimation using eddy covariance when combined with gas concentration measurements. Temperature, relative humidity, and atmospheric pressure are measured from ground level to 130m. Rain gauges are deployed, and solar radiation flux is measured at 40m, separating total and diffuse incoming and reflected radiation from plant cover.

The measured gases include carbon dioxide, water vapor, methane, ozone, and nitrogen oxides, with sampling frequencies ranging from 10 Hz to once every 10 seconds at various heights up to 110 meters. Atmospheric particulate matter and air ions are also monitored using an electrical aerosol spectrometer, which measures particle size distributions from 3 nanometers to 10 micrometers.

In addition to vegetation monitoring, 30m scaffolding towers near the main tower provide direct access to coniferous and deciduous tree branches and host flux measurements. Soil water content is measured at 5, 10, 20, 30, 40, 60, and 100 cm depths at several locations. Soil temperatures are measured at 5 and 10 cm depths.

Figure 3.3 shows the location of the main tower and auxiliary 30m towers (SCT1 and SCT2), used for evapotranspiration and NEE estimation in this work. The figure also depicts the Järvselja forest region and the footprint area of the main tower, calculated using the simple two-dimensional parameterization for Flux Footprint Prediction (FFP) (Mercuri et al., 2023).

3.2 Hydrological Modeling Framework

This section details the hydrological modeling approaches applied in this study. To evaluate the capability of different architectures in representing hemiboreal catchment dynamics, three distinct modeling configurations were implemented:

1. **Conceptual Model (GR4J-Cemaneige):** A physics-based lumped model serving as the hydrological benchmark.

2. **Standalone LSTM:** A pure data-driven deep learning model relying solely on meteorological forcing.

3. **Hybrid LSTM+GR4J:** A physics-informed architecture that integrates conceptual state variables into the neural network.

Additionally, diagnostic tools (In-silico Probe with SVR) were developed to enhance model interpretability and evaluate the learning of physical processes.

3.2.1 Data Preparation

The precipitation time series for Reola was based on data from the two meteorological stations shown in Figure 3.2: Tartu–Tõravere and Võru. These stations provide records of

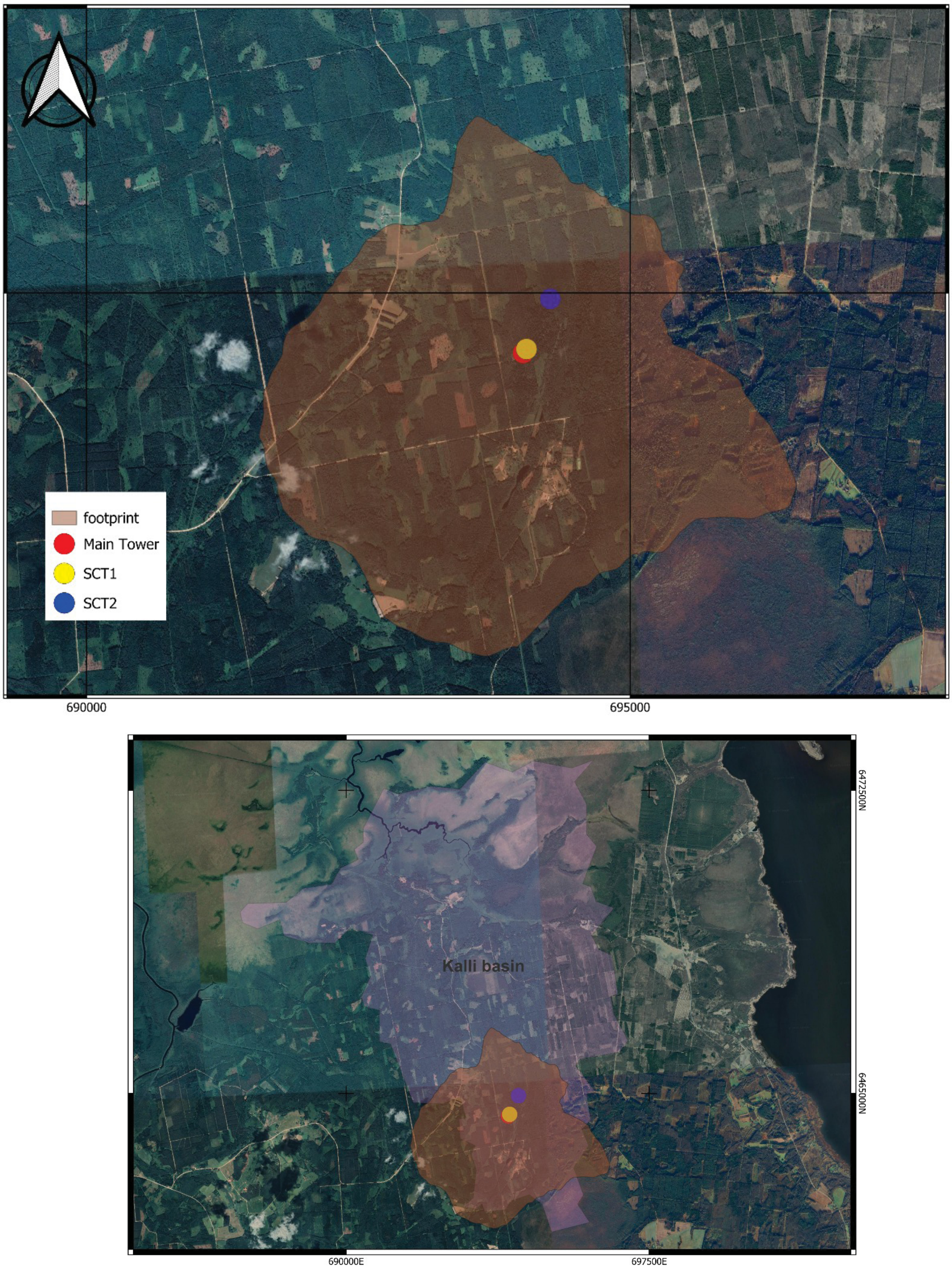

Figure 3.3: Location of the Smear Estonia station: (Top) main tower coverage and scaffold towers (SCT1 & SCT2) at the Järvselja forest; (Botton) main tower footprint in relation to the Kalli basin boundary.

precipitation (rain, snow, and hail) and temperature. Data from the years 2015 to 2021 were aggregated to a daily scale, using the mean of the two stations.

The Reola hydrological station provides discharge data in cubic meters per second ($Q_{m^3/s}$). For the implementation of the models, discharge was converted to millimeters per day ($Q_{mm/day}$) using Equation 3.1 and the catchment area (A_{km^2}):

$$Q_{mm/day} = \frac{Q_{m^3/s} \times 86.4}{A_{km^2}} \tag{3.1}$$

Evapotranspiration inputs were obtained from MODIS (Moderate Resolution Imaging Spectroradiometer) and corrected for the Reola basin based on Eddy Covariance measurements from the SMEAR Estonia station, following the methodology described in Mercuri et al. (2023).

Experimental Implementation

To investigate the role of physical information in deep learning, two distinct LSTM configurations were implemented:

1. **Standalone LSTM (Data-Driven):** This model was fed exclusively with meteorological forcing data (x_t): precipitation, min/max temperature, and evapotranspiration. It relies solely on the network's ability to learn the rainfall-runoff transformation from raw data.
2. **Hybrid LSTM+GR4J (Physics-Informed):** This configuration integrates physical constraints. The input vector x_t includes the meteorological data *plus* the internal state variables simulated by the GR4J model: the production reservoir level ($S(t)$) and the snowpack storage ($G(t)$). This allows the network to utilize the conceptual model's approximation of physical states.

Both architectures utilized a structure of two layers with 16 hidden units and a look-back window (observation time) of 60 days. The models were trained for 5000 epochs, selecting the epoch with the lowest error. The calibration, warm-up, and validation periods were identical to those of the GR4J-Cemaneige model.

3.2.2 LSTM structure

Figure 3.4 shows the macro structure of a cell in the LSTM: each cell receives the cell state (c_{t-1}), the hidden state (h_{t-1}), and an input (x_t) for time step t, with the hidden state defined as the last cell's output. The cell state,represents the system's memory containing information about previous time steps, including what the model decides to keep or change.

The LSTM architecture consists of layers, as demonstrated in Equations 3.2 to 3.8. Given an input sequence $\mathbf{x} = (x_1, x_2, \ldots, x_T)^\top$, each x_t is a vector of model inputs.

$$i_t = \sigma(W_i x_t + U_i h_{t-1} + b_i), \tag{3.2}$$

$$f_t = \sigma(W_f x_t + U_f h_{t-1} + b_f), \tag{3.3}$$

$$g_t = \tanh(W_g x_t + U_g h_{t-1} + b_g), \tag{3.4}$$

$$o_t = \sigma(W_o x_t + U_o h_{t-1} + b_o), \tag{3.5}$$

$$c_t = f_t \odot c_{t-1} + i_t \odot g_t, \tag{3.6}$$

$$h_t = o_t \odot \tanh(c_t). \tag{3.7}$$

(3.8)

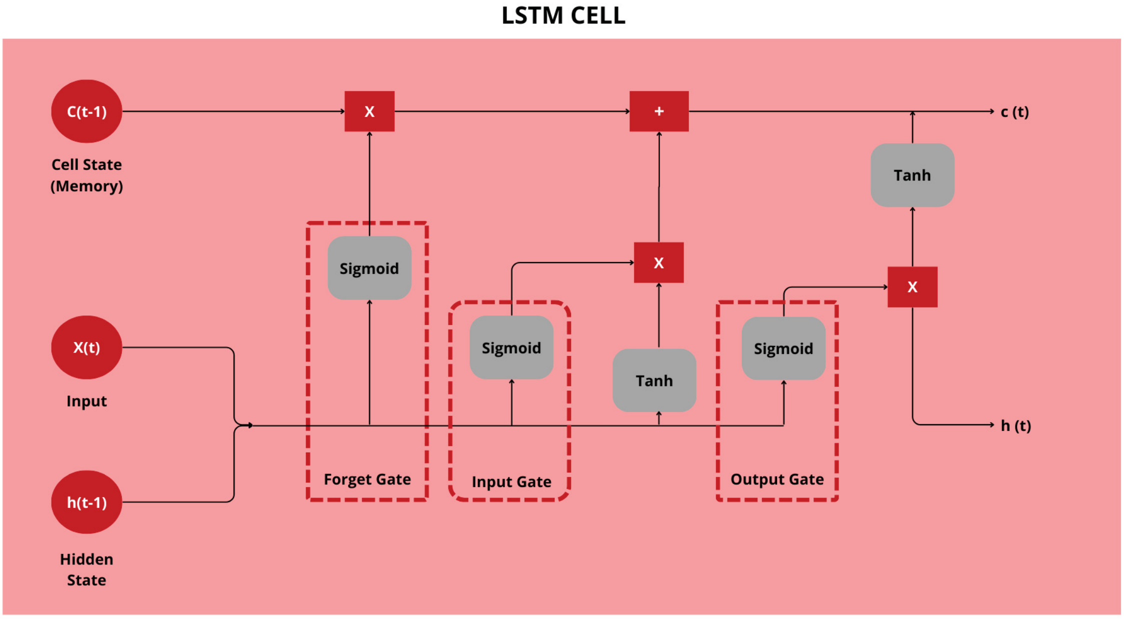

Figure 3.4: Internal structure of a Long Short-Term Memory (LSTM) unit. The diagram shows the flow of information through the cell state ($c(t)$) and hidden state ($h(t)$), as well as the roles of the forget gate, input gate, and output gate. The gates use sigmoid activations to control the flow of information, while the candidate values are regulated by the hyperbolic tangent function (tanh).

In these equations, σ denotes the sigmoid activation function, tanh the hyperbolic tangent, and $\odot$ the element-wise (Hadamard) product. The weight matrices $W_{\{\cdot\}}$, $U_{\{\cdot\}}$ and biases $b_{\{\cdot\}}$ are learnable parameters. The symbol f_t in Equation 3.3 is called the forget gate layer, where the model decides which previous information (h_{t-1}) will be discarded through a sigmoid activation function W_i and b_i represent weights and biases of the function itself. This layer analyzes h_{t-1} and x_t and generates a number between 0 and 1 for each element in the cell state C_{t-1}, where 0 indicates completely forgetting the data and 1 indicates saving it completely.

The next step is to decide which information will be kept in the cell state. Using the activation of a sigmoid function on Equation 3.2 (i_t) called the “input gate layer” , the model decides which values will be updated, and then passed through a hyperbolic tangent activation function on Equation 3.4, creating the output candidate vector g_t that will be added to the cell state. These two activations are combined to update the cell state, reintroducing new data into the cell state to rebalance those that were forgotten in the previous step.

Next, the system's previously made decision is implemented, updating the old state C_{t-1} to the new state C_t through the Equation 3.6. Finally, the cell's output is based on its current state, but in a filtered version. Firstly, a sigmoid activation function o_t 3.5, called the output layer decides which part of the cell state C_t will be considered for the output, and then a hyperbolic tangent (Equation 3.6) function is applied to define the values between -1 and 1, that will create the hidden layer.

3.2.3 Probe

Based on the work of Lees et al. (2022), a physical probe was implemented within the model as a diagnostic tool applied to a pre-trained LSTM. The purpose of the probe is to establish a link between the internal states of the LSTM and a specific environmental variable, allowing us to explore the relationship between the model's learned representations and physical processes.

In this context, a *probe* refers to a diagnostic model designed to analyze the internal representations of an LSTM and assess whether they encode meaningful physical information (Lees et al., 2022). The probe functions as a regression model that maps the LSTM cell states to an external variable of interest. While simple implementations may rely on linear regression, this work adopts Support Vector Regression (SVR) to better capture complex, non-linear relationships at the expense of interpretability.

The application of probes originated in the field of Natural Language Processing (NLP), where they are used to determine whether neural network embeddings contain information associated with semantically meaningful concepts.Adapting this methodology to hydrology, we seek to identify meaningful physical concepts encoded within the LSTM's internal states.

Figure 3.4 illustrates the classical LSTM cell. At the top section of the figure, we can see the cell state memory output ($c(t)$), which is stored at each timestep during the simulation. This vector contains the parameters that the LSTM considers necessary to perform the simulation at that specific timestep. We can then use independent data sources that the LSTM model has never seen before—such as the ERA5 and SMAP datasets—to map $c(t)$ to a corresponding soil moisture value at time t. In this way, we obtain an input series and an output target, enabling us to apply the probe. The probe, implemented using SVR, is trained to map these internal states to observed soil moisture values through supervised learning. However, supervised learning represents a limitation in this context, as our goal is not merely to generate predictions, but to gain insights into the physical processes captured by the LSTM during training.

Figure 3.5 illustrates this behavior. In red, we highlight the cells shown in Figure 3.4, while in yellow (C_t) we represent the cell state at each time step t. In green, we indicate the corresponding target value (S_1) that will be used for probing. During the simulation of streamflow, the C_1 values are stored and subsequently paired with S_1 — for example, soil moisture values from ERA5. We then apply the probe (SVR), shown in blue, to obtain a regression model that relates these variables.

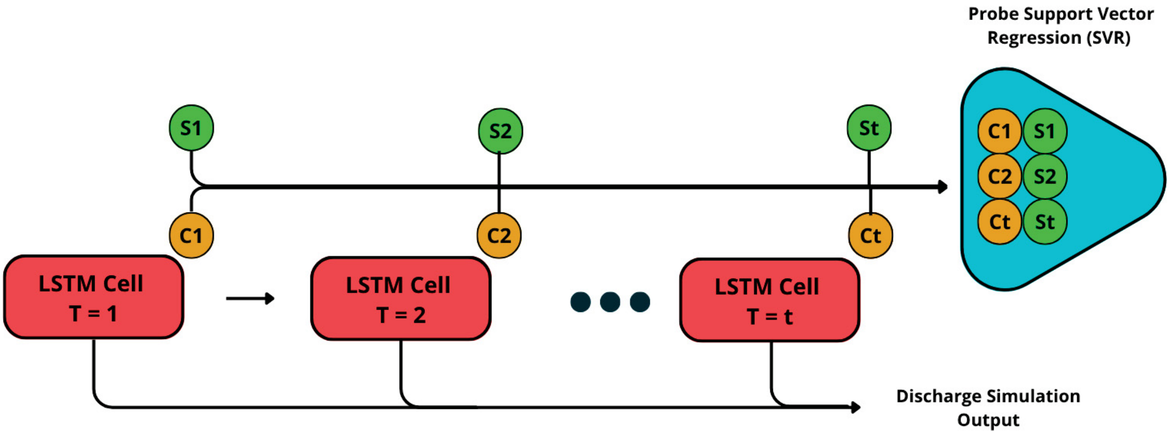

Figure 3.5: Schematic representation of the probe (SVR) applied to the LSTM system. The red blocks represent the LSTM cells, yellow indicates the cell states (C_t) at each time step, and green corresponds to the target values (S_1) used for regression (e.g., soil moisture from ERA5). The blue cell represents the Support Vector Regression (SVR) model fitted between the stored cell states and the target values.

Several differences from the work of Lees et al. (2022) are apparent. Primarily, they employed a linear probe, whereas we used an SVR-based probe on a single, calibrated basin LSTM. This methodological divergence likely accounts for some discrepancies in observed feature. While a linear probe offers simplicity and interpretability, its capacity to capture complex, non-linear relationships within the LSTM's hidden states is limited. Our SVR probe, on the other hand, is designed to model these non-linear dependencies, potentially revealing a more nuanced picture of how the LSTM encodes basin characteristics. Furthermore, the use of a single, calibrated basin LSTM as opposed to an ensemble, might lead to different activation patterns and, consequently, different feature importance. The calibration process, intended to optimize performance for a each basin, could inadvertently emphasize certain features over others.

3.2.4 SVR - Support Vector Regression

The SVR methodology aims to find a function $f(x) = wx + b$ that approximates the training data (x_i, y_i), where x_i are the input vectors, y_i are the corresponding output values, w is the weight vector, and b is the bias. SVR introduces a margin of tolerance, denoted by ϵ (epsilon). The objective is to find a hyperplane (or function) such that most of the training data lies within a "tube" of width 2ϵ around the estimated function, while simultaneously minimizing the model's complexity. Complexity is often measured by the norm of the weight vector, $||w||^2$. This is formalized by the following optimization problem:

$$\min \frac{1}{2}||w||^2 + C\sum_{i=1}^{N}(\xi_i + \xi_i^*) \tag{3.9}$$

subject to the constraints:

$$\begin{gathered} y_i - (wx_i + b) \leq \epsilon + \xi_i \\ (wx_i + b) - y_i \leq \epsilon + \xi_i^* \\ \xi_i, \xi_i^* \geq 0 \end{gathered} \tag{3.10}$$

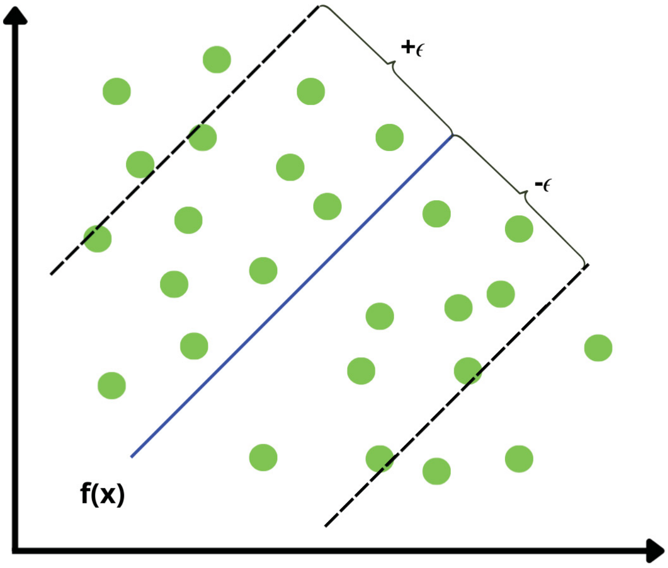

Figure 3.6: A graphical representation of Support Vector Regression. The blue line represents the regression hyperplane (the model), and the dashed lines define the ϵ tube. Data points within this tube incur no loss. The goal of SVR is to find a hyperplane that has most of the data points within this margin while minimizing model complexity.

In these equations, $||w||^2$ represents the model complexity, ϵ defines the width of the error-insensitive zone (the tube), and ξ_i, ξ_i^* are slack variables that allow some data points to fall outside the ϵ-tube, penalized by the regularization parameter C. The term $C\sum(\xi_i + \xi_i^*)$ represents the training error to be minimized. The implicit loss function here is the ϵ-insensitive loss, which does not penalize errors smaller than ϵ.

Essentially, SVR seeks the best trade-off between model complexity (minimizing $||w||^2$) and the amount of error larger than ϵ allowed (minimizing the sum of slack variables, weighted by C). This balance results in a robust model with good generalization capability (as illustrated in Figure 3.6).

3.2.5 Conceptual Hydrological Model GR4J-Cemaneige

By coupling the GR4J and Cemaneige models Fig 3.7, the inputs of the models become: daily precipitation, potential evapotranspiration, maximum, minimum, and mean daily temperatures, and mean basin altitude. Additionally, six calibration constants are required - X_1 (production reservoir capacity in mm), X_2 (inter-basin exchange coefficient in mm/day), X_3 (routing reservoir capacity in mm), X_4 (unit hydrograph time constant in days), the θ_{G1} weighting coefficient for the thermal state of the snowpack, and θ_{G2} (melting coefficient per degree-day in $\frac{\text{mm}}{^{\circ}\text{C}\cdot\text{day}^{-1}}$).The calibration of the GR4J-Cemaneige constantes was made by Dynamically Dimensioned Search (DDS)(Section 3.2.6), all of this can be seen in Figure 3.7, and is further explained in this section.

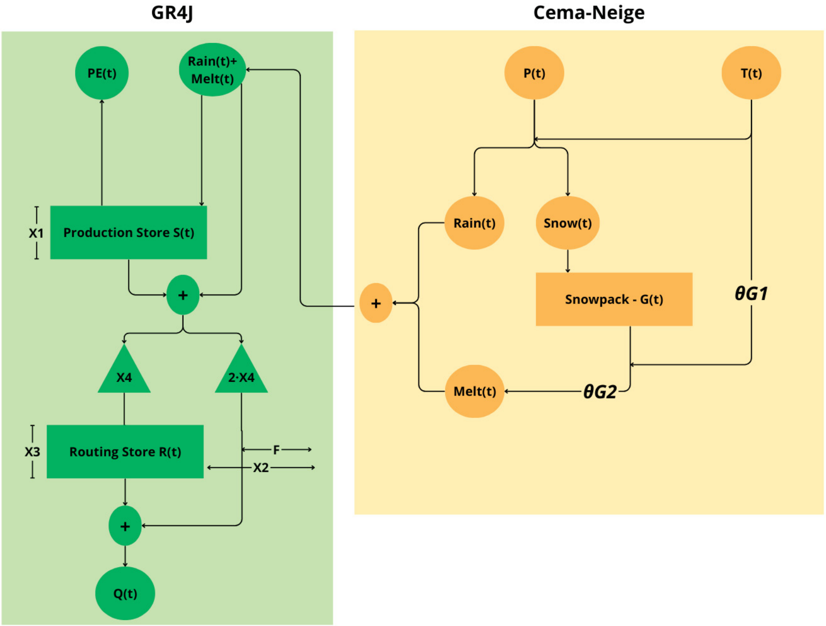

Figure 3.7: On the yellow box, the Cemaneige model is illustrated. In this module, precipitation is directed by temperature inputs to determine which storage will be filled — either the snowpack storage or the total available water input for the GR4J model, shown on the left side of the diagram. The grenn side represents the GR4J model, which uses the inputs from Cemaneige and evapotranspiration data to simulate two types of storage and two unit hydrographs, with the objective of modeling streamflow. The model parameters and constants will be explained in the section.

The Cemaneige model determines the fraction of precipitation that falls as snow. This solid fraction depends on the elevation of the catchment and the temperature conditions. Once this fraction is estimated, the snowfall ($Snow_f$) is calculated as the product of the total precipitation (TP) and the solid fraction (SF):

$$Snow_f = TP \cdot SF \tag{3.11}$$

Consequently, the effective liquid rainfall input, referred to as $Rain$, is obtained by subtracting the snowfall from the total precipitation:

$$Rain = TP - Snow_f \tag{3.12}$$

The model then proceeds to the accumulation phase, in which the computed snowfall is added to the snowpack water equivalent storage, denoted by G:

$$G = G + Snow_f \tag{3.13}$$

Following the accumulation, the thermal state of the snowpack, represented by its cold-content eT_G, is updated. This variable plays a crucial role in determining whether snowmelt can occur. Its update is based on a memory function that incorporates the previous cold-content value and the current mean daily temperature (T_{mean}). The weighting of this update is controlled by the parameter θ_{G2}:

$$eT_G = \theta_{G2} \cdot eT_G + (1 - \theta_{G2}) \cdot T_{mean} \tag{3.14}$$

Potential snowmelt is then calculated using a degree-day method, which is activated only under specific thermal conditions—namely, when the snowpack cold-content has reached thermal equilibrium ($eT_G = 0$) and the mean daily temperature is above freezing ($T_{mean} > 0$). Under these conditions, the potential amount of snowmelt is given by:

$$Potential\ Snowmelt = \theta_{G1} \cdot T\_mean \tag{3.15}$$

However, to ensure physical consistency, this potential snowmelt is limited to the available snowpack G. If the computed value exceeds the current snowpack storage, it is adjusted accordingly:

$$Potential\ Snowmelt = G \tag{3.16}$$

The model then estimates the snow-covered area, which corresponds to the fraction of the basin still covered by snow. This is calculated as a function of the snowpack G and an empirical threshold $G_{threshold}$, defined as 90% of the mean annual snowfall. If the snowpack is below this threshold, the snow-covered area is proportionally reduced:

$$\text{If } G < G_{threshold} : \quad SnowCoveredArea = \frac{G}{G_{threshold}} \tag{3.17}$$

Otherwise, if the snowpack exceeds or equals the threshold, full coverage is assumed:

$$\text{If } G \geq G_{threshold} : \quad SnowCoveredArea = 1 \tag{3.18}$$

Using the estimated snow-covered area, the actual snowmelt is then computed by scaling the potential snowmelt accordingly:

$$Snowmelt = SnowCoveredArea \cdot Potential\ Snowmelt \tag{3.19}$$

After the snowmelt is quantified, the snowpack storage is updated to reflect the melted volume:

$$G = G - Snowmelt \tag{3.20}$$

Finally, the total water input to the hydrological model is determined by summing the effective rainfall and the actual snowmelt:

$$P = Rain + Snowmelt \tag{3.21}$$

The implementation of the rainfall-runoff GR4J model begins with the determination of the net precipitation (P_n) and the residual evapotranspiration (E_n). These variables are calculated by comparing daily total water quantity (P) and potential evapotranspiration (E) inputs. When total water quantity is greater than or equal to evapotranspiration ($P \geq E$), the effective total water quantity is defined as the surplus $P - E$, and there is no evapotranspiration deficit. Conversely, when precipitation is lower than evapotranspiration ($P < E$), all the water is used for evapotranspiration, and the remaining demand is considered a deficit. This leads to the following expressions:

$$P_n = \begin{cases} P - E, & \text{if } P \geq E \\ 0, & \text{otherwise} \end{cases} \qquad E_n = \begin{cases} 0, & \text{if } P \geq E \\ E - P, & \text{otherwise} \end{cases} \tag{3.22}$$

Next, the model simulates the behavior of a production store, which regulates infiltration and evapotranspiration processes. When $P_n > 0$, a portion of the effective precipitation infiltrates into the production store. The infiltrated amount P_s is calculated as a function of the current water level S in the store and the store's maximum capacity X_1 (in mm)

$$P_s = \frac{X_1 \left[1 - \left(\frac{S}{X_1}\right)^2\right] \tanh\left(\frac{P_n}{X_1}\right)}{1 + \frac{S}{X_1} \tanh\left(\frac{P_n}{X_1}\right)} \tag{3.23}$$

on the other hand, if $E_n > 0$, the actual evaporation E_s from the production store is estimated as

$$E_s = \frac{S\left(2 - \frac{S}{X_1}\right) \tanh\left(\frac{E_n}{X_1}\right)}{1 + \left(1 - \frac{S}{X_1}\right) \tanh\left(\frac{E_n}{X_1}\right)} \tag{3.24}$$

The percolation rate (Perc) from the production store to the routing components is calculated by a nonlinear function of the store content:

$$\text{Perc} = S \cdot \left[1 - \left(1 + \left(\frac{4S}{9X_1}\right)^4\right)^{-0.25}\right] \tag{3.25}$$

The storage level is then updated as:

$$S = S_{t-1} - E_s + P_s - \text{Perc} \tag{3.26}$$

The total water volume reaching the routing part of the model (P_r) is given by the sum of percolation and the portion of effective precipitation that did not infiltrate:

$$P_r = \text{Perc} + (P_n - P_s) \tag{3.27}$$

(P_r) is split into two pathways: 90% is routed through Unit Hydrograph 1 (UH$_1$) and 10% through Unit Hydrograph 2 (UH$_2$). Both hydrographs are derived from S-curves defined by a time base parameter X_4 (in days), with UH$_1$ using a base of X_4 days and UH$_2$ of $2X_4$ days.The S-curves for both hydrographs are defined as follows:

$$SH_1(t) = \begin{cases} 0 & \text{for } t \leq 0 \\ \left(\dfrac{t}{X_4}\right)^{5/2} & \text{for } 0 < t < X_4 \\ 1 & \text{for } t \geq X_4 \end{cases}$$

$$SH_2(t) = \begin{cases} 0 & \text{for } t \leq 0 \\ \dfrac{1}{2}\left(\dfrac{t}{X_4}\right)^{5/2} & \text{for } 0 < t < X_4 \\ 1 - \dfrac{1}{2}\left(2 - \dfrac{t}{X_4}\right)^{5/2} & \text{for } X_4 < t < 2X_4 \\ 1 & \text{for } t \geq 2X_4 \end{cases} \tag{3.28}$$

The ordinates of UH_1 and UH_2 are derived from the S-curves:

$$\begin{aligned} UH_1(t) &= SH_1(t) - SH_1(t-1) \\ UH_2(t) &= SH_2(t) - SH_2(t-1) \end{aligned} \tag{3.29}$$

The routed flows from UH_1 and UH_2 are denoted as Q_{UH1} and Q_{UH2}, respectively. The flow from UH enters a nonlinear routing store with water level R. A groundwater exchange term F affects both components and is defined as:

$$F = X_2 \left(\frac{R}{X_3}\right)^{7/2} \tag{3.30}$$

In Equation 3.30 X_2 is a water exchange coefficient and X_3 is the maximum capacity of the routing store. The routing store level R and the routed outflow Q_r are calculated as

$$R = \max(0, R_{t-1} + Q_{UH1} + F) \tag{3.31}$$

$$Q_r = R\left[1 - \left(1 + \left(\frac{R}{X_3}\right)^4\right)^{-0.25}\right] \tag{3.32}$$

the reservoir level at time t is updated by subtracting Q_r from the previous time step value R_{t-1}. Simultaneously, the output from UH_2 is added to the groundwater exchange term F to compute the delayed flow Q_d,

$$Q_d = \max(0, Q_{UH2} + F) \tag{3.33}$$

the total simulated streamflow Q is finally obtained by summing the routed and delayed components:

$$Q = Q_r + Q_d \tag{3.34}$$

3.2.6 Performance Evaluation Metrics and Calibration Algorithms

The **Nash-Sutcliffe Efficiency (NSE)** coefficient is a widely used statistical metric in hydrology to assess the predictive capability of models Nash and Sutcliffe (1970). It quantifies how well the simulated outputs of a model match observed data, specifically comparing the residual variance of the simulated data to the variance of the observed data. NSE values range from $-\infty$ to 1. An NSE of 1 indicates a perfect match between simulated and observed values, while an NSE of 0 suggests that the model is no better than using the mean of the observed data as a predictor. Negative NSE values imply that the observed mean is a superior predictor to the model itself, signaling unsatisfactory performance.

$$NSE = 1 - \frac{\sum_{t=1}^{N}(Q_o^t - Q_m^t)^2}{\sum_{t=1}^{N}(Q_o^t - \overline{Q}_o)^2} \tag{3.35}$$

In equation 3.35, Q_o^t is the observed discharge at time t, and Q_m^t is the modeled discharge at the same time. The term $\overline{Q}_o$ denotes the mean of the observed discharges over the entire period, and N represents the total number of time steps.

Kling-Gupta Efficiency (KGE) is an alternative metric witch integrates three essential statistical components—the correlation coefficient (r), the variability ratio (α), and the bias ratio (β)—into a single multi-objective measure of model performance (Gupta et al., 2009). KGE ranges from $-\infty$ to 1, with a value of 1 indicating perfect agreement between simulations and observations. Unlike NSE, a KGE value of 0 does not correspond to the performance of the observed mean as a predictor; instead, using the mean flow as a predictor results in KGE ≈ -0.41.

$$\text{KGE} = 1 - \sqrt{(r-1)^2 + (\alpha-1)^2 + (\beta-1)^2} \tag{3.36}$$

In the Equation 3.36 r is the linear correlation coefficient between observations (O) and simulations (M); $\alpha = \frac{\sigma_P}{\sigma_O}$ is the variability ratio, defined as the ratio between the standard deviation of the simulated values (σ_M) and that of the observed values (σ_O); and $\beta = \frac{\mu_M}{\mu_O}$ is the bias ratio, which compares the mean of the simulated values (μ_M) to the mean of the observed values (μ_O). This formulation allows for the simultaneous assessment of correlation, variability, and bias, thus providing a more balanced evaluation compared to traditional single-metric approaches.

The **Root Mean Square Error (RMSE)** measures the average magnitude of the differences between values predicted by a model and the actual observed values (Hyndman and Koehler, 2006). It is mathematically defined as the standard deviation of the residuals, which represent the distances between the regression line and the data points. RMSE is often preferred over **Mean Squared Error (MSE)** because it provides a measure of error in the same units as the original data, making it more interpretable. A lower RMSE indicates that the model's predictions are closer to the actual values, signifying higher accuracy. Due to the squaring operation of the differences, RMSE penalizes large errors more severely than small errors.

$$\begin{aligned} \text{RMSE} &= \sqrt{\text{MSE}} \\ \text{MSE} &= \frac{1}{n}\sum_{t=1}^{n}(Q_o^t - Q_m^t)^2 \end{aligned} \tag{3.37}$$

In these equations (3.37), Q_o^t represents the actual value for the t-th observation, Q_m^t is the corresponding predicted value, and n denotes the total number of observations. The Root Mean Square Error (RMSE) provides a measure of the average magnitude of the prediction error, with higher sensitivity to larger errors due to the squaring process in the Mean Squared Error (MSE).

The **Mean Absolute Error (MAE)** is a statistical measure that calculates the average absolute difference between a model's predicted output and the actual observed values Stigler (1986). It quantifies the average magnitude of errors without considering their direction, meaning positive and negative errors don't cancel each other out. MAE is expressed in the same units as the original data, which makes it intuitively interpretable. It's often considered ideal for situations where training data might contain outliers, as it penalizes large errors linearly, making it less sensitive to them compared to RMSE.

$$\text{MAE} = \frac{1}{n}\sum_{t=1}^{n}\left|Q_o^t - Q_m^t\right| \tag{3.38}$$

In equation 3.38, Q_o^t represents the observed value at time t, Q_m^t is the corresponding modeled value, and n is the total number of time steps. The Mean Absolute Error (MAE) measures the average magnitude of the errors in a set of predictions, without considering their direction. It provides a linear score, meaning all individual differences are weighted equally in the average.

Bias refers to the systematic deviation of simulated values from observed values, indicating whether a model tends to consistently overestimate or underestimate the true observations. Unlike random errors, which fluctuate around the true value, bias acts consistently in one direction. A bias of zero indicates an unbiased model. In the context of hydrological modeling, bias can be computed as:

$$\text{Bias} = \frac{1}{n}\sum_{t=1}^{n}(Q_o^t - Q_m^t) \tag{3.39}$$

To express this systematic error in relative terms, the **Percent Bias (pBIAS)** is often used. It quantifies the average tendency of the model to overpredict (positive values) or underpredict (negative values) the observations as a percentage:

$$\text{pBIAS} = 100 \times \frac{\sum_{t=1}^{n}(Q_m^t - Q_o^t)}{\sum_{t=1}^{n} Q_o^t} \tag{3.40}$$

In equations 3.39 and 3.40, Q_o^t and Q_m^t represent the observed and modeled discharges at time t, respectively, and n denotes the total number of observations. While Bias provides the average magnitude and direction of the error, pBIAS offers a normalized perspective, facilitating comparison across datasets.

The **Pearson Correlation Coefficient**, denoted as r, is a measure that quantifies the strength and direction of the linear association between two variables Pearson (1896). It ranges from -1 to +1. A value of +1 indicates a perfect positive linear relationship, -1 indicates a perfect negative linear relationship, and 0 indicates no linear relationship. Negative values imply that as one variable increases, the other decreases.

$$r = \frac{\sum_{i=1}^{N}(Q_m^t - \overline{Q}_m)(Q_o - \overline{Q}_o)}{\sqrt{\sum_{i=1}^{N}(Q_m^t - \overline{Q}_m)^2 \sum_{i=1}^{N}(Q_o - \overline{Q}_o)^2}} \tag{3.41}$$

In Equation 3.41, Q_m^t and Q_o^t are the t-th values of the independent and dependent variables, respectively; $\overline{Q}_m$ and $\overline{Q}_o$ represent their respective means; and N is the total number of observations.

Calibration Strategy: Dynamically Dimensioned Search (DDS)

In this study, the calibration of the GR4J and LSTM models were carried out using a semi-automated approach based on the Dynamically Dimensioned Search (DDS) optimization algorithm. DDS was specifically developed for problems involving a large number of parameters and is distinguished by its implementation simplicity (Tolson and Shoemaker, 2007).

The algorithm includes a perturbation parameter (r), which represents the desired variation in each parameter at every iteration. Additionally, DDS can be applied to discrete, continuous, and/or mixed variables Campos (2017). DDS begins with a global search for optimal solutions. As the iterations progress and better solutions are found, the algorithm increasingly focuses the search on the regions of the parameter space that yielded the best results, thereby reducing the value of the objective function.

Although DDS is a stochastic global search algorithm and does not guarantee the identification of a global optimum, it was selected due to its computational efficiency and its ability to handle a large number of input parameters.

3.3 Water Balance Closure and Subsurface Water Storage Variation

The water balance of a watershed can be comprehensively described by the differential equation

$$\frac{dS}{dt} = P - ET - Q + (D + I) \tag{3.42}$$

which represents the conservation of mass by accounting for the major hydrological fluxes. In this formulation, $\frac{dS}{dt}$ denotes the instantaneous rate of change in water storage within the system, P is precipitation, ET is evapotranspiration, Q is river discharge per unit area, D represents deep aquifer flow, and I stands for net interbasin water exchange:

In practical hydrological applications, the terms related to deep aquifer exchange (D) and interbasin flow (I) are often poorly constrained due to limited data availability. Consequently, these components are frequently omitted to simplify the analysis. When applying this balance over discrete time steps, such as daily intervals, the equation can be integrated to yield a simplified discrete form, representing the net change in water storage (ΔS_i) for a given time step i:

$$\Delta S_i = P_i - ET_i - Q_i \tag{3.43}$$

It is commonly assumed that, over long periods and large spatial scales, the net change in storage averages out to near zero ($\overline{\Delta S} \approx 0$). However, at finer temporal resolutions—such as daily or seasonal scales—this assumption does not hold, as short-term fluctuations in storage can be substantial and highly relevant for ecohydrological processes. The term ΔS_i thus quantifies the terrestrial water storage variation over time, integrating multiple subsystems of the hydrological cycle. This variation is especially informative when assessing the coupling between surface–subsurface water availability and ecohydrological responses, including groundwater recharge, soil water dynamics, and vegetation water stress.

Following Mercuri et al. (2023), ΔS_i can be further decomposed into distinct hydrological compartments that collectively describe surface and subsurface water storage within the catchment

$$\Delta S_i = \Delta GW_i + \Delta SM_i + \Delta SWE_i + \Delta SW_i \tag{3.44}$$

where ΔGW_i is the change in groundwater storage, ΔSM_i the change in soil moisture, ΔSWE_i the change in snow water equivalent, and ΔSW_i the change in surface water, including water retained in rivers, lakes, and interception by vegetation. This decomposition enables a more refined understanding of where and how water is stored or depleted in the system, particularly under climate-driven extremes such as droughts or snowmelt events.

3.4 Data Acquisition and Processing of Carbon Fluxes

3.4.1 Instrumentation and Data Sources

Measurements of carbon dioxide (CO_2) and water vapor (H_2O) fluxes were primarily collected from the SMEAR Estonia station's Main Tower at a height of 70 meters. To ensure a continuous long-term time series for Net Ecosystem Exchange (NEE) estimation spanning from 2015 to 2025, these primary observations were supplemented by data from two auxiliary scaffolding towers (SCT1 and SCT2), with sensors located at 30 meters. This redundancy was critical to cover periods of instrument maintenance or malfunction at the main tower.

Raw high-frequency data (10–20 Hz) from these sensors—including wind speed vectors and gas concentrations—were processed to derive key turbulent fluxes, friction velocity, and humidity. Additionally, to complement the observational dataset for gap-filling procedures, radiation data were retrieved from the Copernicus Atmosphere Monitoring Service (CAMS) reanalysis dataset (Gschwind et al., 2019). The temporal coverage of each sensor and the identified data gaps are illustrated in Figure 3.8.

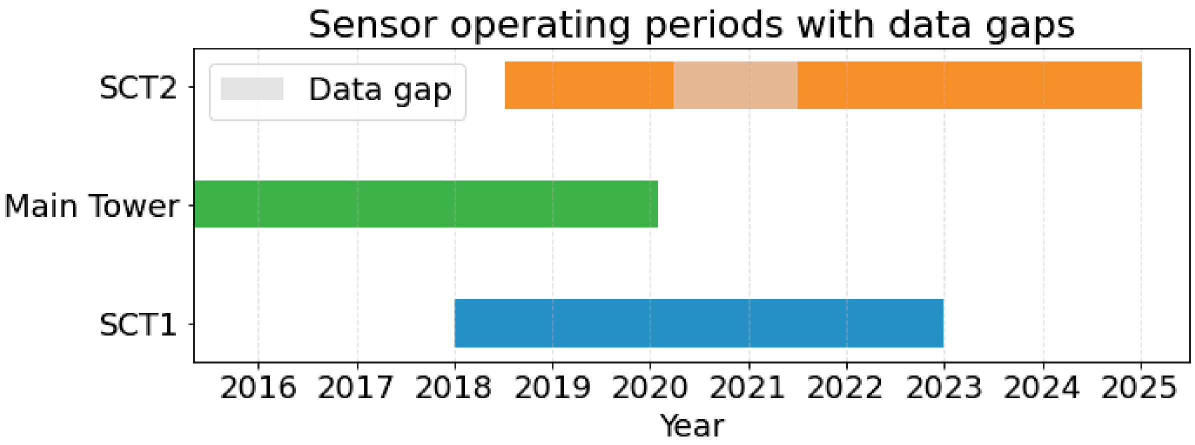

Figure 3.8: Sensor operating periods and data gaps for the Main Tower and auxiliary scaffolding towers (SCT1 and SCT2). The hierarchical combination of these sources allowed for the construction of a continuous time series from 2015 to 2025.

3.4.2 Bias Correction and NEE time series ensemble

Constructing a unified time series from multiple sensors requires careful harmonization to avoid artifacts caused by instrumental differences. A hierarchical approach was adopted: the Main Tower provided the baseline data from 2015 to 2020, while the auxiliary tower (SCT2) covered the period from 2018 to 2025. A critical data gap identified in the primary series between March 2020 and June 2021 was filled using data from the SCT1 station.

To merge these datasets into a single consistent time series, a bias correction procedure was applied to the auxiliary (SCT1) data using the Quantile Mapping (QM) method (Wood et al., 2004; Teng et al., 2015). The QM approach aligns the cumulative distribution function (CDF) of the predictor variable (SCT1) to match the CDF of the reference variable (Main Tower). This ensures that the statistical properties (mean, variance, and quantiles) of the corrected series match the baseline observations, correcting systematic errors while preserving temporal rank correlation. The correction model was trained using the overlapping period between the towers (2018–2020).

3.5 Eddy Covariance Theory and Flux Partitioning

3.5.1 Eddy Covariance Principles

To properly discuss the eddy covariance method, some fundamental concepts must be introduced. The eddy covariance technique is based on the Reynolds decomposition Burba (2013). The description of turbulent motion requires decomposing the time series of any atmospheric variable ζ into its mean component $\overline{\zeta}$ and its fluctuating component ζ'. This is known as the Reynolds decomposition and is written as:

$$\zeta = \overline{\zeta} + \zeta' \tag{3.45}$$

The conservation of any scalar or vector quantity ζ in the atmosphere can be expressed as:

$$\underbrace{\frac{\partial \rho_d \zeta}{\partial t}}_{\text{(I)}} + \underbrace{\vec{\nabla} \cdot (\vec{u}\, \rho_d\, \zeta)}_{\text{(II)}} + \underbrace{K_\zeta\, \Delta\, (\rho_d\, \zeta)}_{\text{(III)}} = \underbrace{S_\zeta}_{\text{(IV)}} \tag{3.46}$$

where ρ_d is the dry air density, $\vec{u}$ is the wind velocity vector, K_ζ is the molecular diffusivity of ζ, and S_ζ represents source or sink terms for ζ.

Assuming steady-state conditions (neglecting the time derivative), horizontal homogeneity (neglecting horizontal gradients), and a coordinate system where $\overline{v} = 0$ and $\overline{w} = 0$, the mass conservation equation allows for the estimation of vertical fluxes. The turbulent fluxes of CO_2 (F_{CO_2}) and H_2O (F_{H_2O}) were calculated as the covariance between vertical wind fluctuations (w') and fluctuations in gas concentration:

$$F_{CO_2} = \mathrm{cov}(w', CO_2') \tag{3.47}$$

$$F_{H_2O} = \mathrm{cov}(w', H_2O') \tag{3.48}$$

This method allows us to quantify gas exchange between the surface and the atmosphere. In the case of CO_2, partitioning the net flux into its main components—Gross Primary Production (GPP) and Ecosystem Respiration (R_{eco})—provides further insight into ecosystem carbon dynamics.

3.5.2 Flux Partitioning Approaches

Partitioning was performed using the REddyProc software (Wutzler et al., 2018), utilizing both nighttime- and daytime-based approaches to robustly gap-fill the series.

Nighttime-Based Approach

According to Reichstein et al. (2005), the Nighttime-Based approach utilizes nighttime measurements of ecosystem respiration to estimate daytime rates. Equation 3.49 from Lloyd and Taylor (1994) was used to calculate respiration (R_{eco}) as a function of temperature (T):

$$R_{eco}(T) = R_{eco,ref}\, e^{E_0\left(\frac{1}{T_{ref}-T_0} - \frac{1}{T-T_0}\right)} \tag{3.49}$$

where E_0 is the temperature sensitivity and $R_{eco,ref}$ is the respiration at a reference temperature ($T_{ref} = 15°C$). The parameter T_0 is fixed at $-46.02°C$. The parameters are estimated in moving windows (typically 14 days) to account for seasonal acclimation of the respiratory processes.

Daytime-Based Approach

The Daytime-Based approach follows Lasslop et al. (2010), partitioning NEE by modeling the photosynthetic response to light using a rectangular hyperbolic light–response function, modified to include temperature-dependent respiration:

$$\mathrm{NEE} = \frac{\alpha \beta R_g}{\alpha R_g + \beta} + R_{\mathrm{eco}}(T) \tag{3.50}$$

where R_g is global radiation, α is canopy light use efficiency, and β is the maximum CO_2 uptake rate. To account for atmospheric water stress, β is modeled as a function of Vapor Pressure Deficit (VPD) (Körner, 1995):

$$\beta = \begin{cases} \beta_0 \cdot e^{-k(VPD - VPD_0)} & \text{if } VPD > VPD_0 \\ \beta_0 & \text{if } VPD \leq VPD_0 \end{cases} \tag{3.51}$$

where VPD_0 is fixed at 10 hPa. This explicit inclusion of VPD is crucial for capturing the depression of GPP during heatwave events, such as the one observed in 2018.

3.6 Soil moisture and water level datasets

To understand the hydrological dynamics of the study area, we used a combination of modeled and observed data for soil moisture and water levels. Specifically, we incorporated remotely sensed soil moisture products from the ERA5 reanalysis and the SMAP mission, along with in-situ water level measurements from a newly installed sensor at the SMEAR Estonia station. The idea is to integrate these datasets with the probe and assess whether the LSTM model is learning the physical characteristics of the basin.

The **ERA5** (Hersbach, 2017) reanalysis dataset, produced by the Copernicus Climate Change Service at ECMWF (European Centre for Medium-Range Weather Forecasts), provides hourly estimates of atmospheric, land, and oceanic climate variables on a global scale, covering the period from 1940 to the present. It is spatially set on a 31 km grid and resolves the atmosphere using 137 vertical levels from the surface up to the mesosphere(80 km). For this study, we downloaded the hourly version of this dataset for the Kalli basin, covering the period from January 1, 2020, to April 1, 2025. The associated volumetric soil water content product (Hersbach et al., 2023) defines the surface at 0 cm and models the soil using a four-layer structure: Layer 1 (0–7 cm), Layer 2 (7–28 cm), Layer 3 (28–100 cm), and Layer 4 (100–289 cm).

The product SMAP Enhanced L2 Radiometer Half-Orbit 9 km EASE-Grid Soil Moisture, Version 6 (O'Neill et al., 2023), developed by NASA's **Soil Moisture Active Passive (SMAP)** mission launched in January 2015, provides high-resolution global mapping of soil moisture and freeze-thaw state using an L-band radar and radiometer. SMAP collects brightness temperature data at a 9 km resolution every 3 hours, which is processed into various soil moisture products, ranging from L1 (raw data) to L4 (highest level of post-processing). For this study, data corresponding to the period from January 1, 2023, to April 1, 2025, were used. The specific product employed is identified as SPL2SMP_E.

The **CAMS Clear-Sky Global Horizontal Irradiation (GHI)** product (Gschwind et al., 2019), part of the Copernicus Atmosphere Monitoring Service (CAMS), provides historical solar radiation time series under clear-sky conditions from 2004 to the present. These data are generated using the ECMWF integrated forecasting system, which assimilates large volumes of observational data. In this study, we used CAMS GHI data as input for the modeling framework, specifically covering the period from June 2024 to April 2025 for the SMEAR main tower location (58.27° N, 27.27° E).

Water level sensor (model TL231)

The water level sensor was installed near the main tower of the SMEAR station (Figure 3.9), directly under the ground. The equipment used was the TL231 model (Figure 3.10), a "throw-in" type level transmitter, suitable for continuous measurements in liquid media.The implementation consists of a PVC pipe with holes spaced every 10 cm to allow water to enter, covered by a filter to prevent the entry of solid materials that could clog the tube. The device was calibrated using a water reservoir, where the calibration was performed by varying the height of the water level above the sensor. The following heights (in cm) were tested: 0, 11, 20, 30, 50, 70, 100, and 105.

Based on the corresponding millivolt (mV) values, a linear regression was performed to relate the water level to the millivolt readings provided by the device. The resulting linear regression was:

$$y \text{ (cm)} = V \text{ (mV)} \times 4.14 - 229.15 \tag{3.52}$$

Figure 3.10: The Water level sensor (model TL231

The sensor was installed at a depth of 1.2m in order to capture variations in the water table or superficial accumulation of water around the tower, allowing direct comparison with the results obtained by simulation, soil moisture sensors, and hydrological storage estimates derived from hydrological models.

Figure 3.9: Water level sensor installed: on the left, its components and assembly procedure; in the center and on the right, the sensor installed near the SMEAR tower.

Chapter 4

Climatological analysis

Estonia, located in the mixed forest sub-region of the Atlantic continental temperate zone, is influenced by the transition between the continent and the Baltic Sea. Its summers are moderately warm (average July temperature between 16 and 17 °C) and the winters are moderately cold (average February temperature between -2.5 and -7 °C). The extreme temperatures recorded range from 35.6 °C to -36.7 °C. The average annual precipitation is between 550 and 700 mm, with uniform seasonal variation throughout the country: February and March are the driest months, while July and August have the highest precipitation rates (Estonian Environment Agency, 2025) To compare data used in this study with regional climatic norms, monthly temperature and precipitation data from ERA5 (1940-2025) were collected and analyzed for the Kalli basin. Metrics derived from this data follow the climatic characteristics described by Estonian Environment Agency (2025), showing an average July temperature of 17.86 °C, an average February temperature of -5.79 °C, average annual precipitation of 701.93 mm, with February being the driest and August the wettest month.

The climatological analysis was performed using the GR4J input data for the period 2015–2025. Monthly average temperature, radiation, relative humidity, and precipitation were calculated and compared against a long-term ERA5 climatology, allowing the computation of anomalies. The temperature anomalie were obtained by subtracting the 85-year ERA5 monthly climatological means (representing a reference climate) from the corresponding monthly means of the GR4J dataset. Figure 4.1 summarizes this analysis through boxplots of monthly temperature, radiation, and relative humidity, as well as bar plots of temperature and precipitation anomalies. The results highlight the clear seasonal temperature pattern with colder conditions during the winter months (December to February) and increased radiation during late spring and summer (May to July), when relative humidity is substantially lower. The anomalies indicate that winters during 2015–2025 were on average 0.4°C warmer, and summers 0.2°C colder, compared to the long-term climatology.

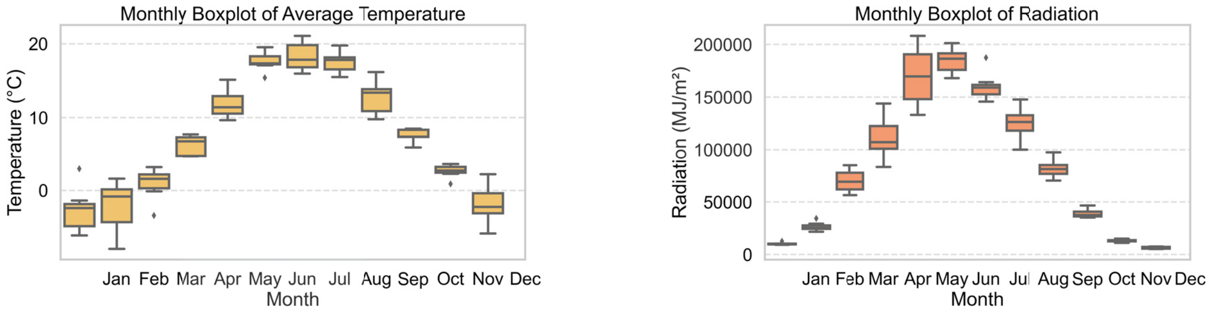

(a) Monthly boxplot of average temperature (°C).

(b) Monthly boxplot of radiation (MJ/m²).

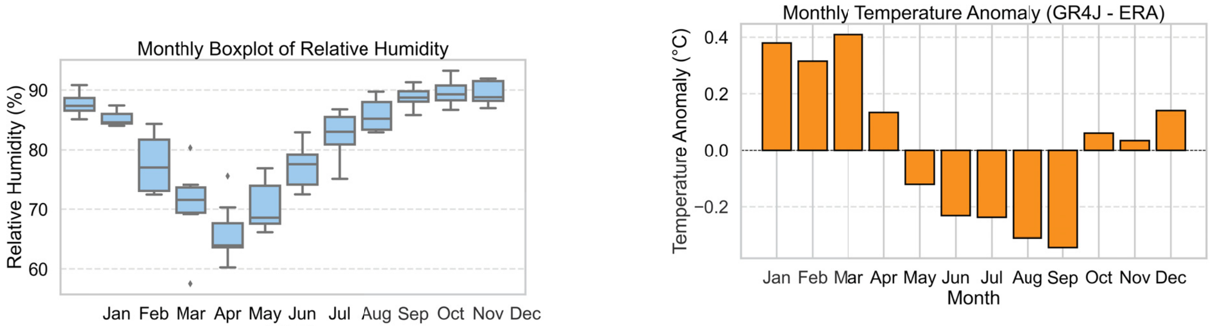

(c) Monthly boxplot of relative humidity (%).

(d) Monthly temperature anomaly (GR4J - ERA5) (°C).

Figure 4.1: Monthly climatological analysis for 2015–2025. Boxplots show the seasonal cycle of temperature, radiation, and relative humidity. Bar plots present temperature anomalies calculated relative to the 85-year ERA5 climatology.

Figure 4.2 displays monthly precipitation and evapotranspiration on the blue and red lines respectivamente. Both exhibit similar trends, except during winter when evapotranspiration approaches zero, and between August and November when precipitation increases. The hatched region which shows minimum and maximum values indicates lower evapotranspiration variability, when compared with precipitation. The black line shows the values of ERA5 historical data mean monthly data.

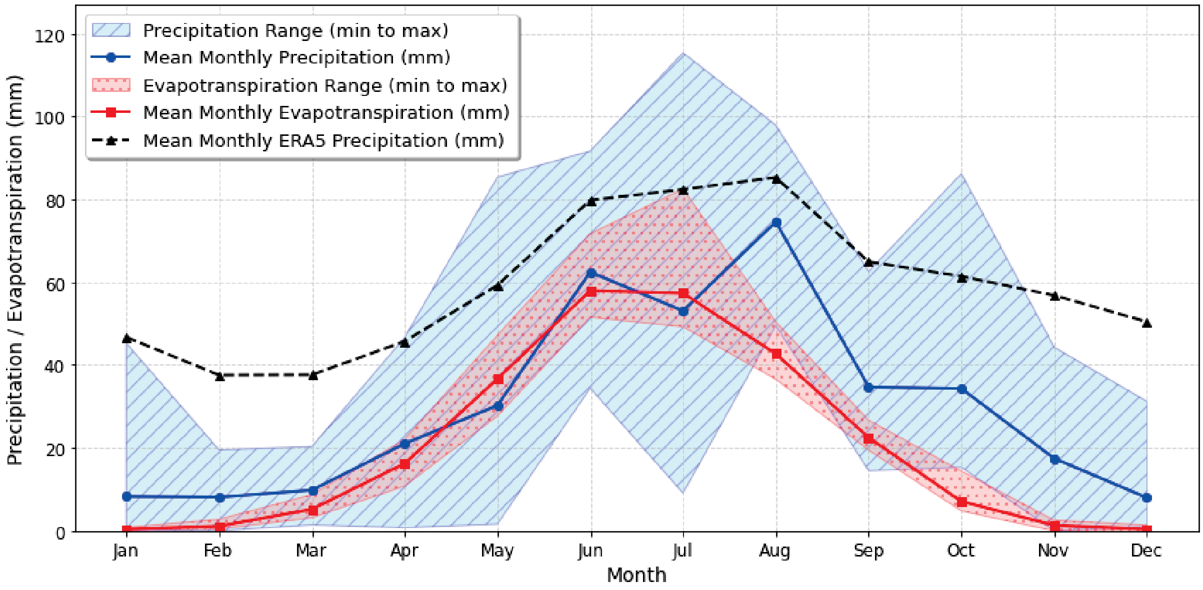

Figure 4.2: Monthly precipitation and evapotranspiration climatology (2015–2025) over the Kalli basin. Lines show mean values; hatched areas represent the interannual range. The dashed black line shows ERA5 mean precipitation over 85 years.

In Figure 4.3, the annual precipitation is presented. Between 2018 and 2024, the average precipitation was 381 mm, the mean temperature was 7.4 °C, and the total evapotranspiration was 250 mm. The year 2018 exhibited the most contrasting values in the series, while 2017 recorded the highest precipitation. The growing period during these years averaged 160 days, ranging from 140 to 173 days depending on the year. The growing season began when the temperature exceeded 5 °C for at least three consecutive days and ended when it dropped below 5 °C for more than three consecutive days.

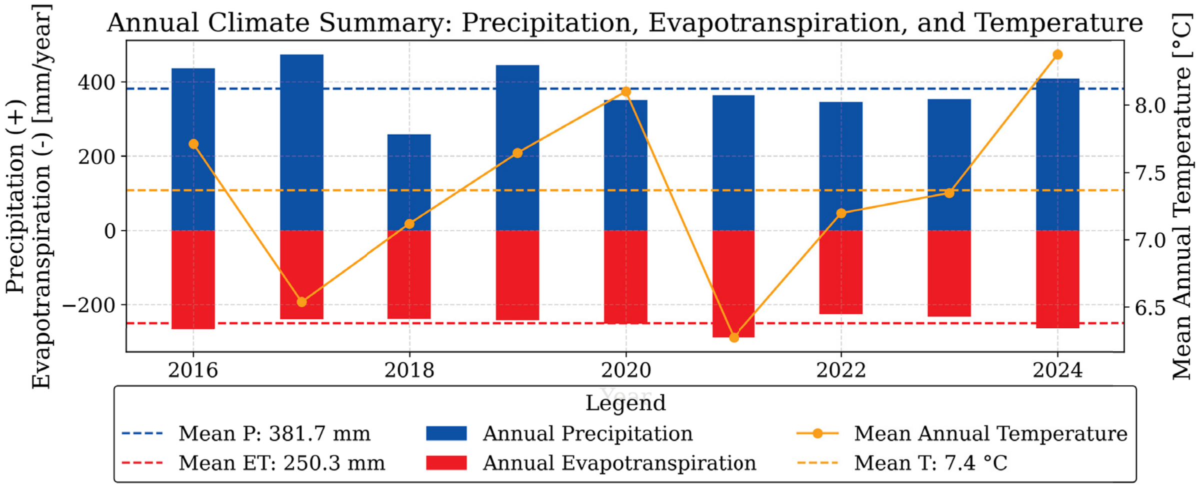

Figure 4.3: Annual accumulated precipitation and evapotranspiration, and mean annual temperature in the Kalli basin, based on meteorological station data for the 2016–2024 period, together with the corresponding long-term annual means.

Considering the 2018 heatwave event mentioned in 2.2, Figures 4.4 and 4.5 illustrate the Kalli basin's precipitation and temperature patterns. In 2018, accumulated precipitation was generally low when compared to the usual, only reaching typical values in April, August and

September. Daily temperatures oscillated significantly around the average, with notably low temperatures in February and high temperatures during summer.

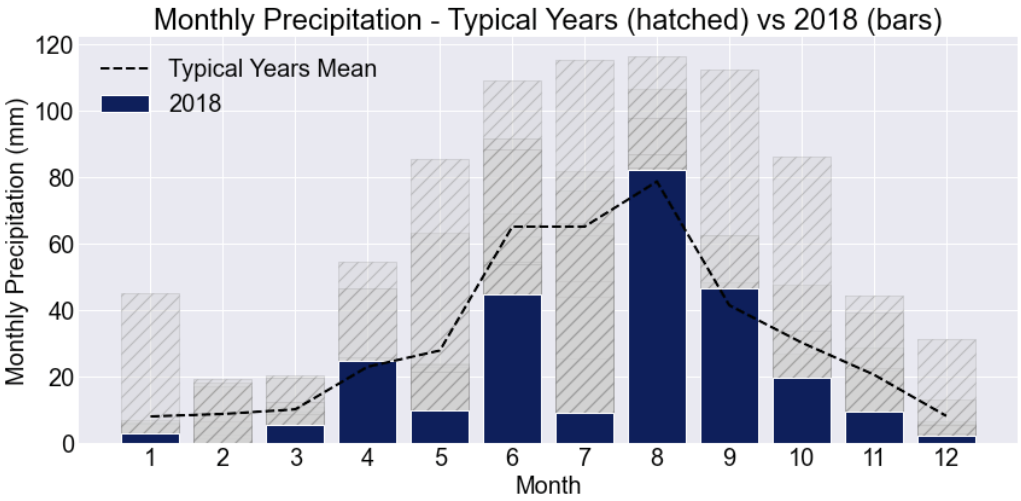

Figure 4.4: Monthly accumulated precipitation for the climatological mean (15-year meteorological station data; black bars) and for 2018 based on meteorological station observations (blue bars). The black line represents the mean values from the meteorological stations.

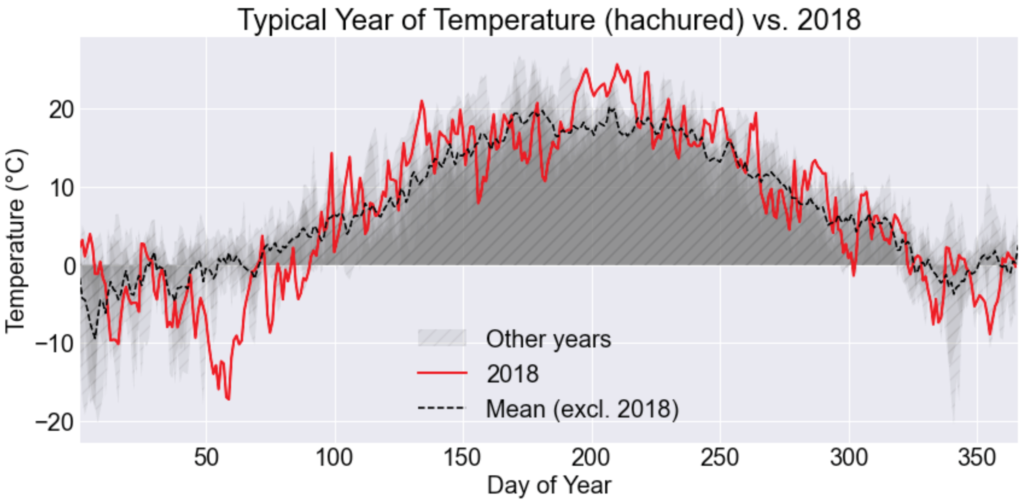

Figure 4.5: Daily temperature climatology based on 15-year meteorological station, with shaded areas representing interannual variability, compared to observed daily temperatures from meteorological stations in 2018.

Chapter 5

Results

Before calculating performance metrics, the physical parameters obtained during the calibration of the conceptual model. For the Reola watershed, the calibrated parameters of the GR4J-Cemaneige were: X_1 (production store capacity) = 340 mm; X_2 (groundwater exchange) = -2.5 mm/day; X_3 (routing store capacity) = 68 mm; X_4 (unit hydrograph time base) = 2.3 days. Regarding the snow module, the weighting coefficient for the snowpack thermal state was θ_{G1} = 0.48, and the degree-day melting coefficient was θ_{G2} = 2.4 mm $°\mathrm{C}^{-1}$ d^{-1}. These values reflect a catchment with significant storage capacity (X_1) and a tendency for groundwater loss to deep aquifers or neighboring basins (negative X_2)

The combined approach using **LSTM+GR4J** delivered the best overall performance among the tested models, showing a clear improvement over both the standalone LSTM and the conceptual GR4J. As presented in Figure 5.1 (a) and detailed in Table 5.1, the hybrid model achieved a **Nash–Sutcliffe Efficiency (NSE)** of **0.887**, surpassing the LSTM (0.827) and the GR4J (0.503). The **Kling–Gupta Efficiency (KGE)** also confirmed this superior performance, with a value of **0.890** compared to 0.852 for the LSTM and 0.631 for the GR4J, indicating that the hybrid model provided a more balanced representation of correlation, bias, and variability in the simulated streamflow. Furthermore, the **LSTM+GR4J** reduced both the absolute bias (**Bias** = -0.005) and the percentage bias (**PBIAS** = -0.91%) relative to the standalone models, highlighting a minimal tendency to either overestimate or underestimate discharge values.

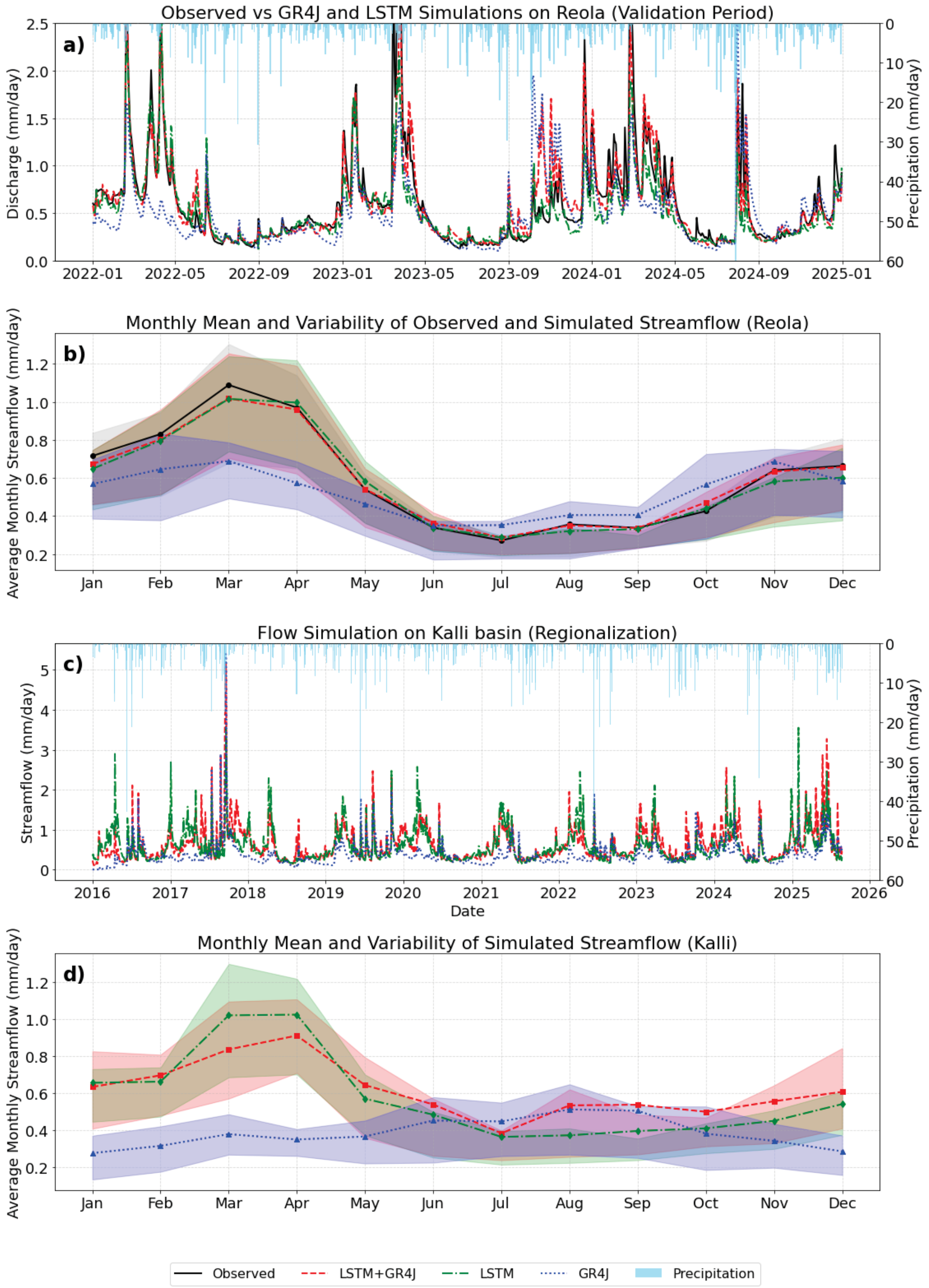

Figure 5.1: Hydrograph analysis of the Reola and Kalli basins. (a) Daily time series comparing observed streamflow (black line) with simulations from the LSTM (dashed red line) and GR4J (dotted blue line) models for the Reola basin in 2020. The light blue bars on the secondary y-axis represent daily precipitation. (b) Monthly mean streamflow for observed data from the Reola basin (black line) and its simulations (red and blue lines), showing the interquartile range (IQR) as shaded areas to indicate variability. (c) Daily streamflow simulations for the Kalli basin from the LSTM and GR4J models, with corresponding daily precipitation (light blue bars). (d) Monthly mean streamflow for the Kalli basin based on LSTM and GR4J simulations, with shaded areas representing the interquartile range (IQR) to show monthly variability.

Table 5.1: Performance metrics of GR4J, LSTM, and hybrid LSTM+GR4J streamflow for the Reola basin.

Metric	GR4J	LSTM	LSTM+GR4J
NSE	0.503	0.827	0.887
KGE	0.631	0.852	0.890
RMSE	0.331	0.195	0.158
MAE	0.194	0.104	0.081
Bias	-0.074	-0.018	-0.005
PBIAS (%)	-12.33	-3.11	-0.91
Pearson (r)	0.728	0.911	0.942
R^2	0.503	0.827	0.887

Figure 5.1(c) presents the streamflow simulation results for both the GR4J-CemaNeige and LSTM implementations in the Kalli basin. Initially, it can be observed that both models are capable of representing potential flow variations in the basin, aligning well with major precipitation peaks. The GR4J-CemaNeige model proves to be more conservative in its response to precipitation, requiring a larger water storage within the system to generate significant oscillations in the simulated flow levels. As a consequence, it tends to convert a smaller portion of water into surface runoff compared to the LSTM model. Conversely, the LSTM model demonstrates greater responsiveness to smaller variations in water storage within the system. The behavior of the LSTM+ model is similar to that of the standard LSTM, although it exhibits more pronounced seasonal variations.

Figures 5.1 (b) and (d) provide comparison of the monthly mean streamflow and its variability. Figure (b) shows the observed streamflow for the Reola basin alongside its simulated values from the LSTM and GR4J models. In contrast, Figure (d) presents the monthly mean simulated streamflow for the Kalli basin from the same models, since no observed data is available for this location.

By comparing these two plots, we can observe distinct hydrological behaviors and model performances between the two basins. For the Reola basin, both the observed data and the LSTM simulation show a clear and pronounced seasonality, with significant peaks and valleys reflecting high and low flows throughout the year. In contrast, the GR4J model for Reola, while capturing the overall seasonal trend, tends to produce a more smoothed series, with less variation between the maximum and minimum flows.

5.0.1 Terrestrial Water Storage Dynamics

The time series of soil moisture content simulated with the probe (Figure 5.2) reveal clear improvements in simulation accuracy when coupling the GR4J model with the LSTM architecture. Across all soil layers, both models capture the temporal dynamics and overall trends of observed soil moisture; however, the hybrid LSTM+GR4J consistently achieves higher correlation and lower normalized error.

In the surface layer (SWVL1, 0–7 cm), the hybrid model attains $r = 0.93$ and NRMSE = 8%, outperforming the pure LSTM ($r = 0.80$, NRMSE = 13%). Similar behavior is observed in the second layer (SWVL2, 7–28 cm), where correlation increases to $r = 0.96$ with a NRMSE of 7%. At intermediate depth (SWVL3, 28–100 cm), both models show strong agreement with observations ($r > 0.97$), while in the deepest layer (SWVL4, 100–289 cm) performance decreases, especially for the pure LSTM ($r = 0.68$, NRMSE = 21%). These results indicate that the hybrid structure is particularly effective in capturing moisture variations in the upper and intermediate layers, where soil–atmosphere interactions are more pronounced.

The comparison between simulated and observed water level data (Figure 5.3) highlights the ability of both probe-LSTM-based model to reproduce the general temporal dynamics of the sensor signal. Despite some discrepancies during the dry period, the pure LSTM model achieves excellent agreement with the observed series ($r = 0.94$, NRMSE = 7%), indicating a strong capacity to learn the nonlinear relationships governing subsurface water dynamics. Conversely, the hybrid LSTM+GR4J exhibits a lower correlation ($r = 0.77$, NRMSE = 14%).To contextualize these results, the daily water storage change (ΔS, shown in yellow) provides a physical baseline derived from the water balance. While the ΔS trajectory corroborates the seasonal drying trend observed by the sensor from May to August, it exhibits a smoother behavior characteristic of system-level aggregation. The LSTM's ability to capture the high-frequency fluctuations—which deviate from the smooth water balance curve—suggests that the data-driven model successfully encodes local hydraulic responses that are not explicitly resolved by the conceptual water balance calculation.

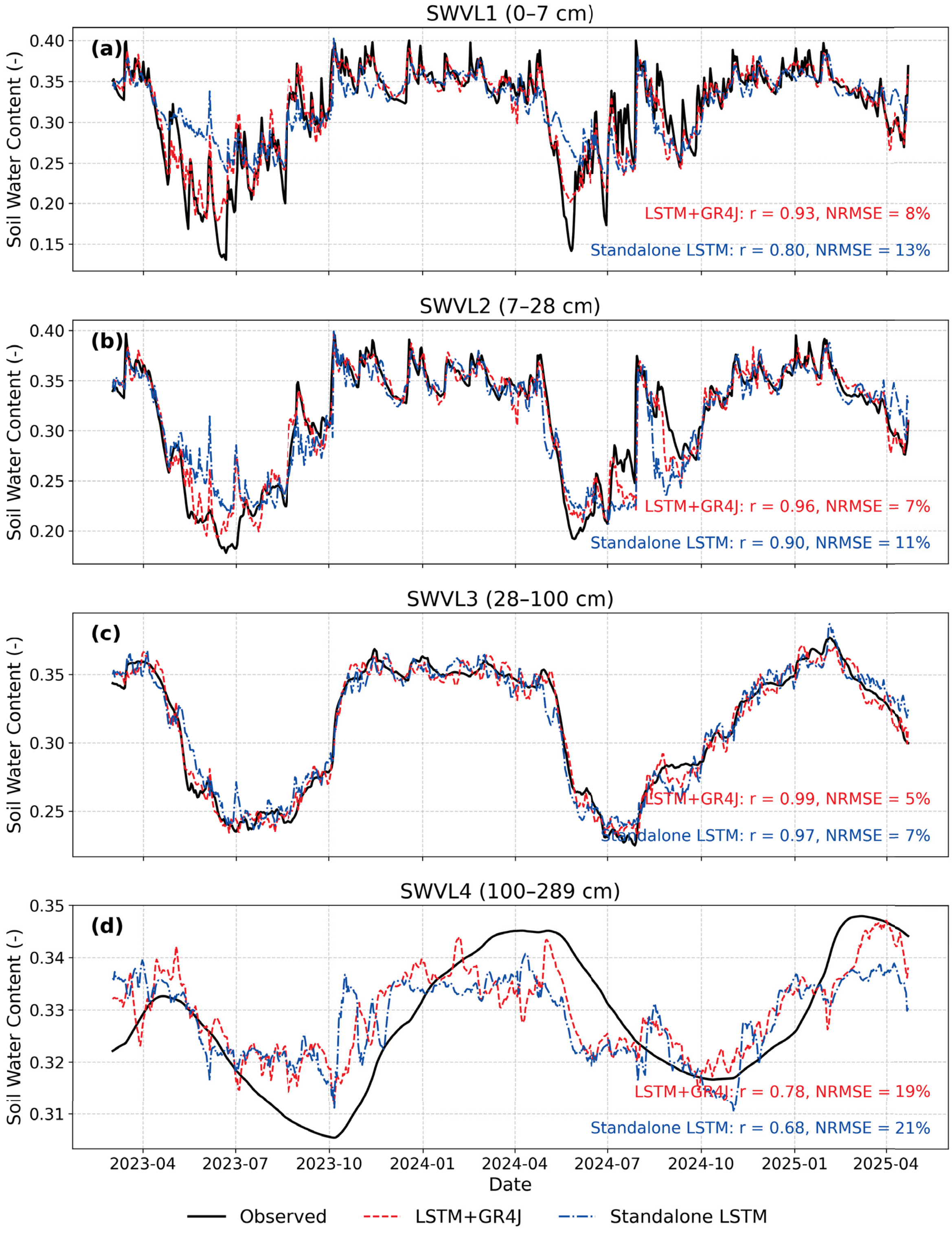

Figure 5.2: This figure presents a comparison between observed soil water content from ERA5-Land,and the simulated soil water dynamics from the LSTM probe and the GR4J conceptual model’s stores. Panels (a) through (d) display the soil water content (dimensionless, ranging from 0 to 1) at different depths from ERA5-Land: SWVL1 (0–7 cm) represents the uppermost layer; SWVL2 (7–28 cm) the shallow subsurface; SWVL3 (28–100 cm) the intermediate root zone; and SWVL4 (100–289 cm) the deeper soil layers.

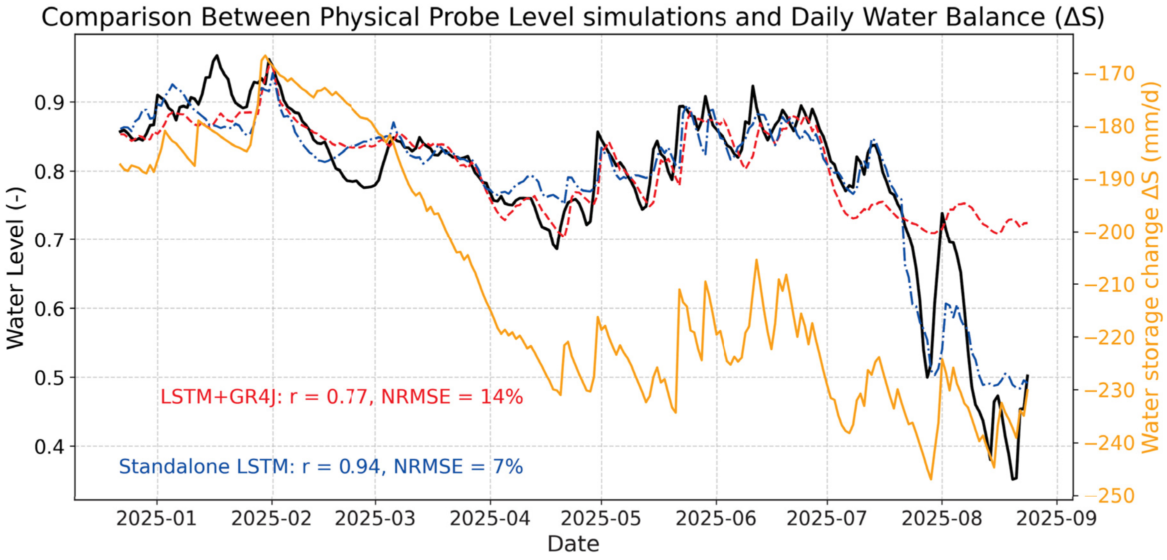

Figure 5.3: Validation of the *in-silico* probe against *in-situ* water level measurements. The plot compares the normalized observed water level signal from the TL231 sensor (black line) with the internal cell state representations from the pure LSTM (blue dashed line) and hybrid LSTM+GR4J (red dashed line) models. The strong correlation indicates the LSTM's capacity to implicitly learn subsurface water dynamics.

5.0.2 Net Ecosystem Exchange

The analysis of Net Ecosystem Exchange (NEE) is central to quantifying the carbon balance of the Järvselja hemiboreal forest. This section presents results derived from a decadal eddy-covariance dataset spanning 2015–2025, with emphasis on the effects of gap-filling procedures and the characterization of seasonal and diurnal carbon exchange patterns.

After applying nighttime- and daytime-based gap-filling methodologies to reconstruct missing NEE observations, annual cumulative values were computed for both the original series (NEE_{orig}) and the final corrected series (NEE_f). Table 5.2 summarizes these annual totals.

Table 5.2: Annual cumulative Net Ecosystem Exchange (NEE) values for the original (uncorrected) and gap-filled series.

Year	NEE_{orig}	NEE_f
2015	-288.19	-161.08
2016	-362.58	-292.76
2017	-409.36	-431.93
2018	-138.98	11.31
2019	-163.89	-120.65
2020	-115.07	-32.55
2021	-278.46	-244.91
2022	-415.17	-303.67
2023	-400.97	-304.83
2024	-359.28	-235.92

In most years, the corrected series exhibits systematically less negative values than the uncorrected series, indicating that the absence of gap-filling leads to an overestimation of the ecosystem's carbon sequestration capacity. This bias is primarily associated with missing data during nighttime periods characterized by low atmospheric turbulence, when eddy-covariance measurements tend to underestimate ecosystem respiration. The most pronounced discrepancy occurs in 2018: while the uncorrected series suggests that the forest remained a net carbon sink, the corrected data demonstrate a breakdown of sink behavior.

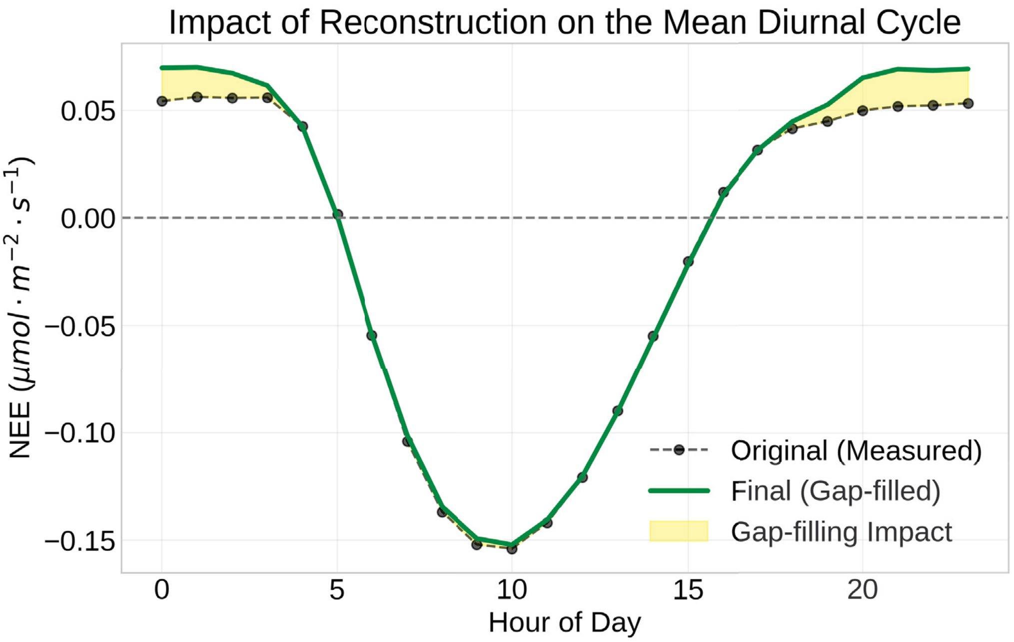

Figure 5.4: Impact of data reconstruction on the mean diurnal cycle of NEE. The yellow shaded area quantifies the difference between the measured (raw) series and the final (corrected/gap-filled) series.

The impact of the gap-filling procedures on sub-daily dynamics is illustrated in Figure 5.4, which compares the mean diurnal cycle of measured and corrected NEE. A near-perfect agreement is observed during daytime hours, approximately between 05:00 and 17:00, when atmospheric turbulence is sufficient to ensure reliable flux measurements. In contrast, substantial deviations arise during nighttime and transition periods (early morning and dusk), highlighted by the yellow shaded area. During these intervals, the corrected series displays systematically higher (more positive) NEE values, reflecting the compensation for underestimated ecosystem respiration under stable atmospheric conditions.

Figures 5.5provide a multi-scale perspective on NEE dynamics throughout the study period. The central fingerprint heatmap relates hour of day to annual seasonality and clearly delineates the characteristic "sequestration eye" during midday hours (approximately 08:00–16:00) in spring and summer. During these periods, the ecosystem acts as a strong carbon sink driven by peak gross primary production. Conversely, positive NEE values dominate nighttime hours and the winter months, indicating net carbon release associated with suppressed photosynthesis and sustained autotrophic and heterotrophic respiration.

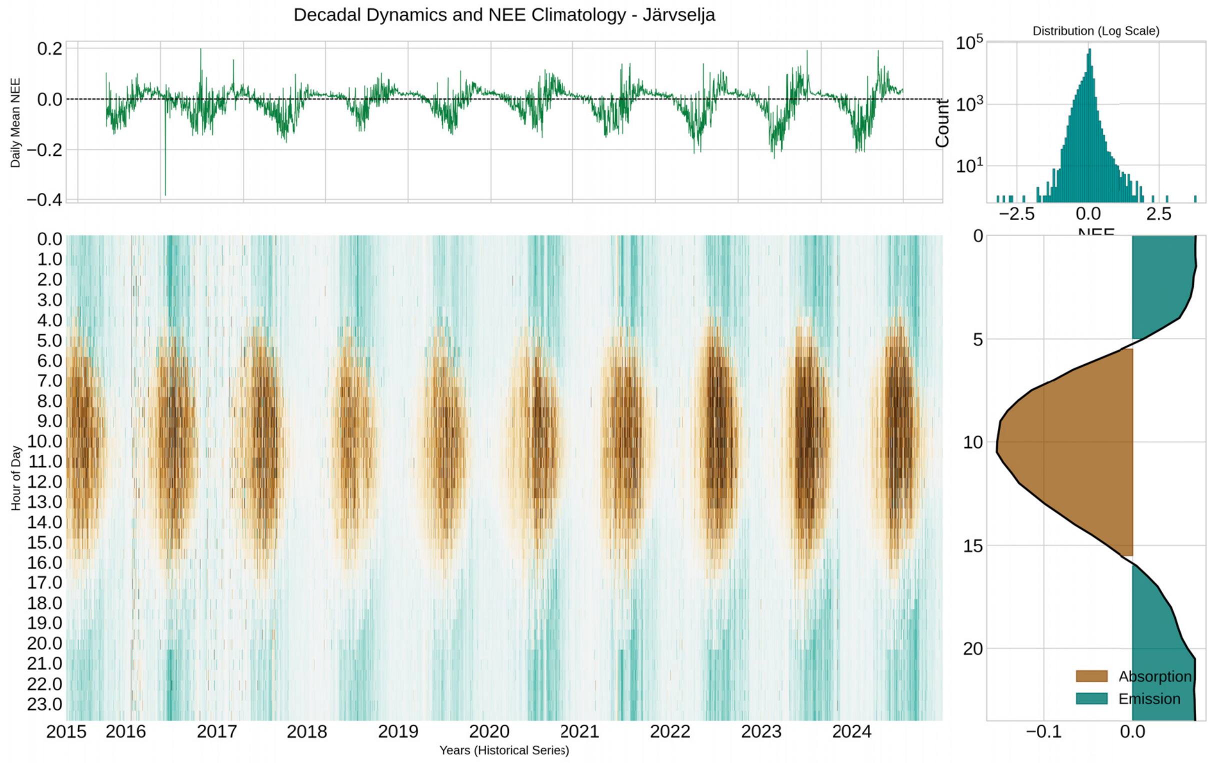

Figure 5.5: Composite NEE climatology (2015–2025). The central heatmap correlates the hour of the day with annual seasonality, highlighting peak sequestration windows (green) and phases of winter metabolic dormancy (white).

The upper panel of the composite figure shows the daily mean NEE time series, revealing pronounced interannual variability. The disruption of summer carbon uptake during the 2018 heatwave is evident as a marked attenuation of the typical seasonal sequestration signal. The accompanying histogram (log-scaled) illustrates the statistical distribution of NEE values, characterized by a high frequency of near-neutral exchanges and a long negative tail corresponding to high-intensity sequestration events. Finally, the marginal diurnal profile summarizes the mean partitioning between carbon uptake and release over a typical day, reinforcing the strong asymmetry between daytime assimilation and nighttime respiration.

5.0.3 Validation of Carbon Flux Partitioning

Before analyzing the net ecosystem exchange dynamics, the reliability of the flux partitioning methods was assessed. The performance of the two standard approaches—Nighttime-Based and Daytime-Based—was evaluated through a comparative analysis of the typical annual cycles of Gross Primary Production (GPP) and Ecosystem Respiration (R_{eco}).

As illustrated in Figure 5.6, both methodologies produce highly consistent estimates. Although the models rely on distinct premises—with the Nighttime approach extrapolating respiration from nighttime data and the Daytime approach fitting photosynthetic parameters to light response curves—the agreement is remarkable. Both approaches effectively capture the strong seasonality of the ecosystem, with fluxes peaking during the summer months (DOY 150–250). This high correspondence reinforces confidence in the validity of the gap-filled dataset used in the subsequent analyses.

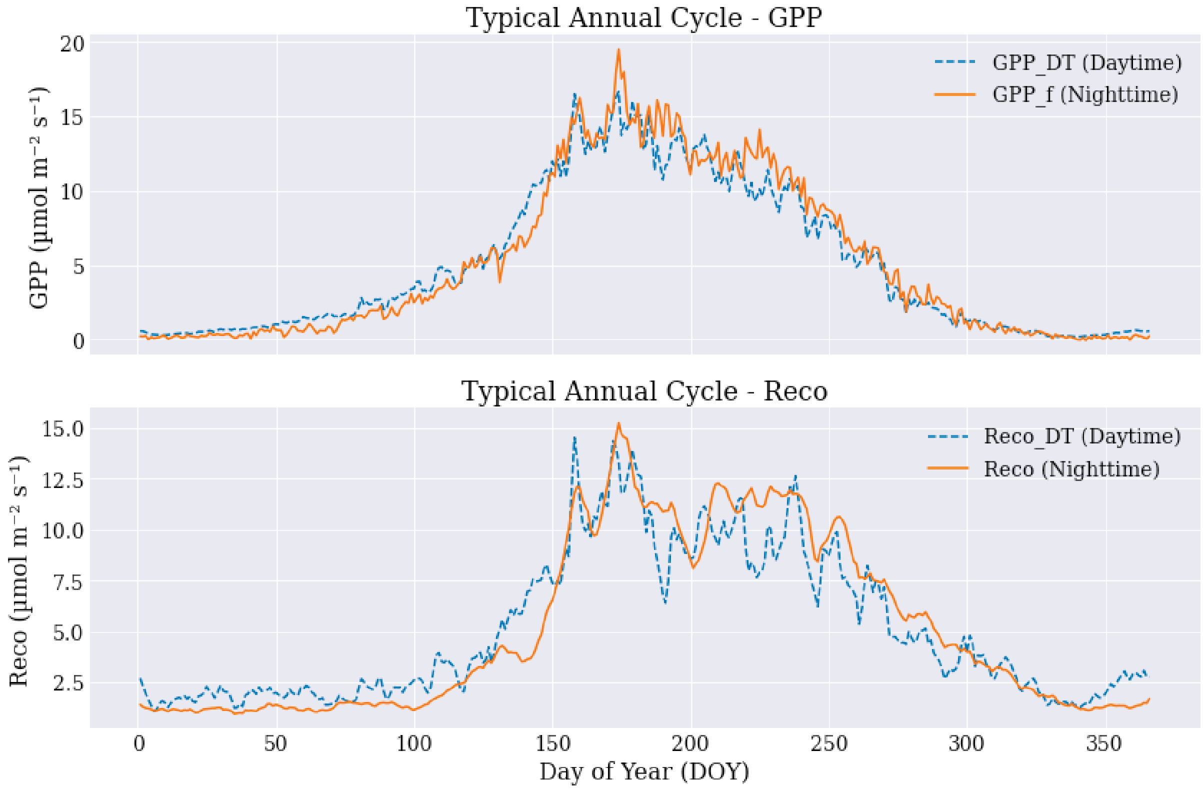

Figure 5.6: Typical annual cycle of partitioned carbon fluxes, Gross Primary Production (GPP) and Ecosystem Respiration (R_{eco}), based on data from 2015 to 2025. The top panel compares GPP derived from Daytime-Based (dashed line) and Nighttime-Based (solid line) approaches. The bottom panel shows the corresponding R_{eco} estimates. The strong agreement between independent methodologies validates the robustness of the derived fluxes.

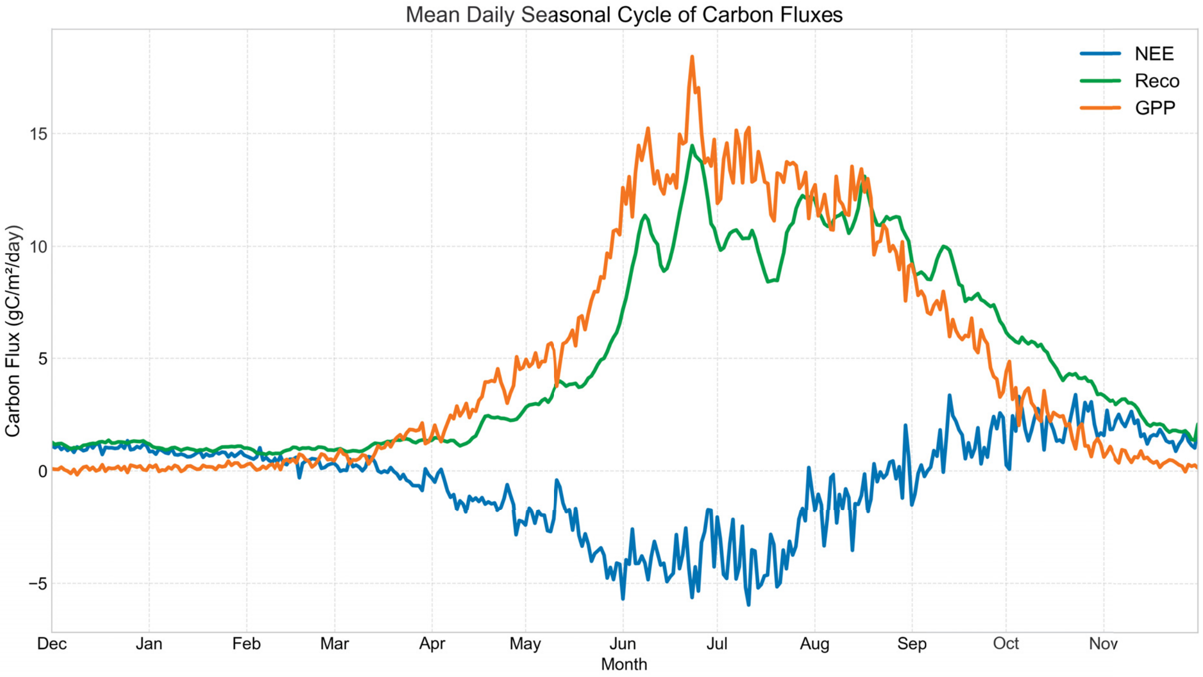

Figure 5.7: Mean daily seasonal cycle of carbon fluxes (Net Ecosystem Exchange - NEE, Ecosystem Respiration - R_{eco}, and Gross Primary Productivity - GPP) at Järvselja, Estonia. These daily accumulated values, calculated from data spanning 2015 to 2025, illustrate the typical annual patterns of carbon exchange between the hemiboreal forest ecosystem and the atmosphere. Negative NEE values indicate the ecosystem acts as a net carbon sink (carbon uptake), while positive values indicate a net carbon source (carbon release).

Figure 5.7 illustrates the mean seasonal cycle of Net Ecosystem Exchange (NEE), Ecosystem Respiration (R_{eco}), and Gross Primary Productivity (GPP). These daily accumulated values, calculated from data spanning 2015 to 2025, represent the typical carbon flux patterns in the Estonian ecosystem. The figure clearly shows the ecosystem acting as a net carbon sink (negative NEE) during spring and summer, when GPP significantly exceeds R_{eco}. Conversely, during autumn and winter, carbon uptake diminishes considerably, leading to the ecosystem transitioning into a carbon source (positive or near-zero NEE) due to reduced photosynthetic activity and sustained respiration.

The carbon flux dynamics for the drought year of 2018, in comparison with the long-term typical mean and the interannual variability range, are presented in Figure 5.8. The daily evolution (left panels) reveals a substantial suppression of photosynthetic activity during the vegetative peak (approximately from DOY 150 to 250). The 2018 GPP (red line) drops significantly below the typical mean (dashed black line), reflecting the physiological stress imposed by the drought conditions. Although ecosystem respiration (R_{eco}) also exhibited a decrease—likely due to soil moisture limitations constraining microbial activity—the reduction in GPP was more pronounced. Consequently, the NEE signal shifted towards positive values during mid-summer, indicating a substantial reduction in the forest's net carbon uptake capacity during the peak of the drought.The integrated impact of this event is quantified in the cumulative fluxes shown in the right panels of Figure 5.8. The cumulative GPP for 2018 presents a severe deficit relative to the historical average, which was not fully offset by the concurrent decline in respiration. As a result, the cumulative NEE trajectory deviates sharply from the typical sink behavior. While the forest typically functions as a robust carbon sink (accumulating negative NEE values by year-end), the

2018 trajectory ends near zero, effectively turning the ecosystem into a carbon-neutral system or a very weak sink for that specific year.

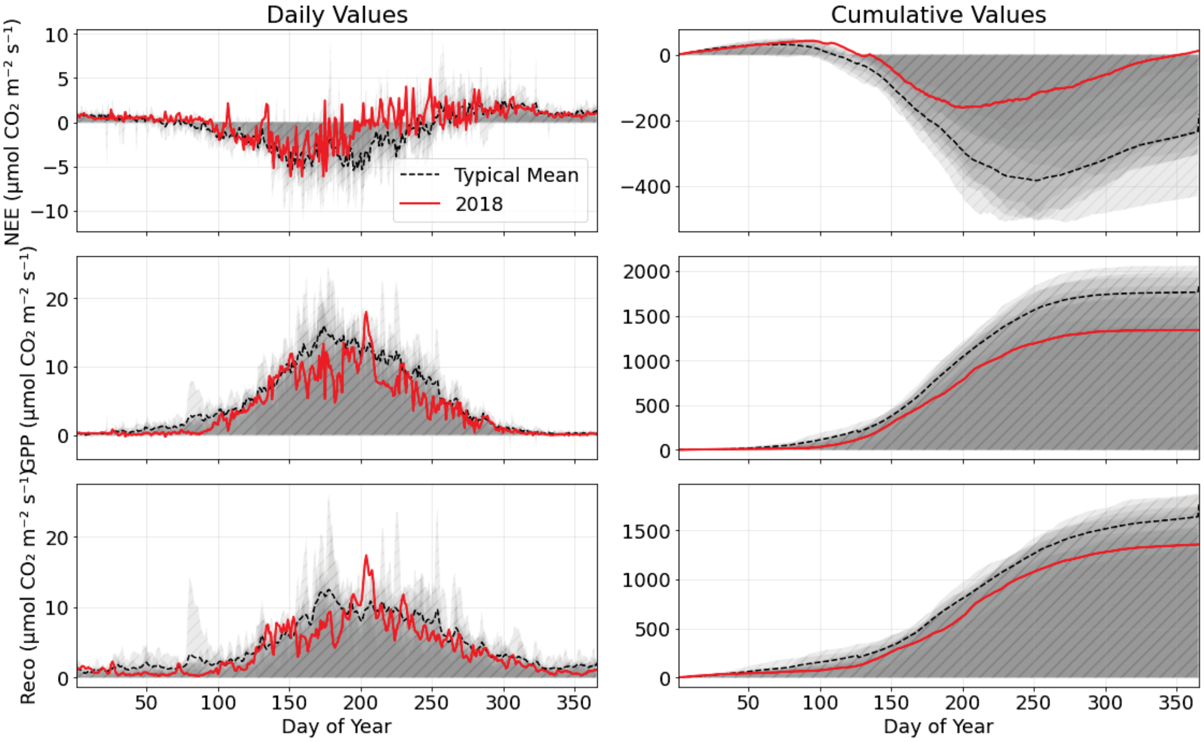

Figure 5.8: Comparison of carbon flux dynamics during the 2018 drought versus the long-term climatology. The left column displays the mean daily seasonal cycle, while the right column shows the cumulative annual fluxes for Net Ecosystem Exchange (NEE), Gross Primary Production (GPP), and Ecosystem Respiration (R_{eco}). The red line represents the 2018 specific trajectory, the black dashed line shows the typical mean (2015–2025), and the grey shaded area represents the interannual variability range. Note the significant suppression of GPP during the summer months (left) and the resulting stagnation of the cumulative NEE sink function (right).

To explicitly quantify the coupling between hydrological availability and ecosystem productivity, Figure 5.9 contrasts the cumulative water balance (ΔS) with the cumulative NEE for the drought year (2018) against the climatological mean. A synchronous divergence is observed starting at DOY 150. As the cumulative water balance (cyan line) plunges into a severe deficit—reaching approximately -150 mm due to the cessation of precipitation—the cumulative NEE trajectory (red line) stagnates. This flattening of the NEE curve marks the point where soil moisture depletion became the limiting factor for photosynthesis. Unlike a typical year (black dashed line), where the ecosystem continues to act as a sink throughout summer, in 2018 the system transitioned into a net source in the second half of the year, ending with a positive cumulative NEE value. This confirms that the exhaustion of soil water storage directly inhibited the forest's capacity to sequester carbon.

Expanding the analysis to the interannual scale, Figure 5.10 aggregates the daily fluxes to reveal long-term trends from 2015 to 2024. The time series reveals two distinct hydrological-carbon regimes. The pre-drought period (2015–2018, red trends) exhibits a rapid hydrological drying (ΔS slope = -39.61 mm yr^{-1}) strongly correlated with a weakening of the carbon sink capacity (NEE slope = $+35.95$ gC m^{-2} yr^{-1}). This trend culminates in the 2018 pivot point. However, the post-drought period (2020–2024, orange trends) indicates a recovery phase: as the water balance stabilized and showed a slight wetting trend (ΔS slope = +7.31), the ecosystem's carbon uptake capacity began to recover, with NEE trending back towards stronger sink values (slope = −46.67). This "V-shaped" pattern in both variables underscores the high sensitivity and resilience of the Järvselja forest to interannual hydroclimatic variability.

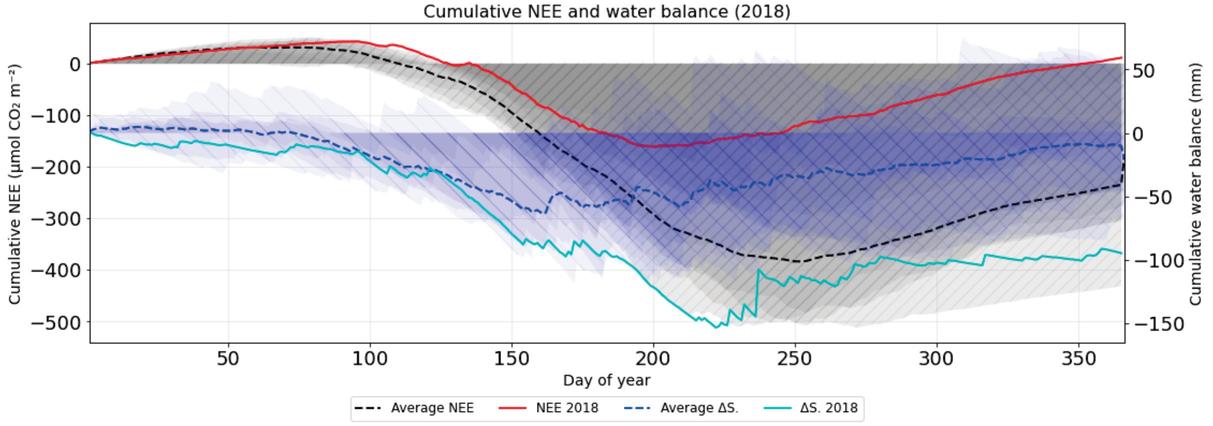

Figure 5.9: Coupling between water availability and carbon uptake during the 2018 drought. The graph compares the Cumulative Net Ecosystem Exchange (NEE) (left axis) and the Cumulative Water Balance ($\Delta S = P - ET - Q$) (right axis). The red and cyan lines represent the 2018 specific trajectories for NEE and ΔS, respectively, while the dashed lines represent the long-term averages. The grey shaded area indicates the cumulative NEE range for other years.

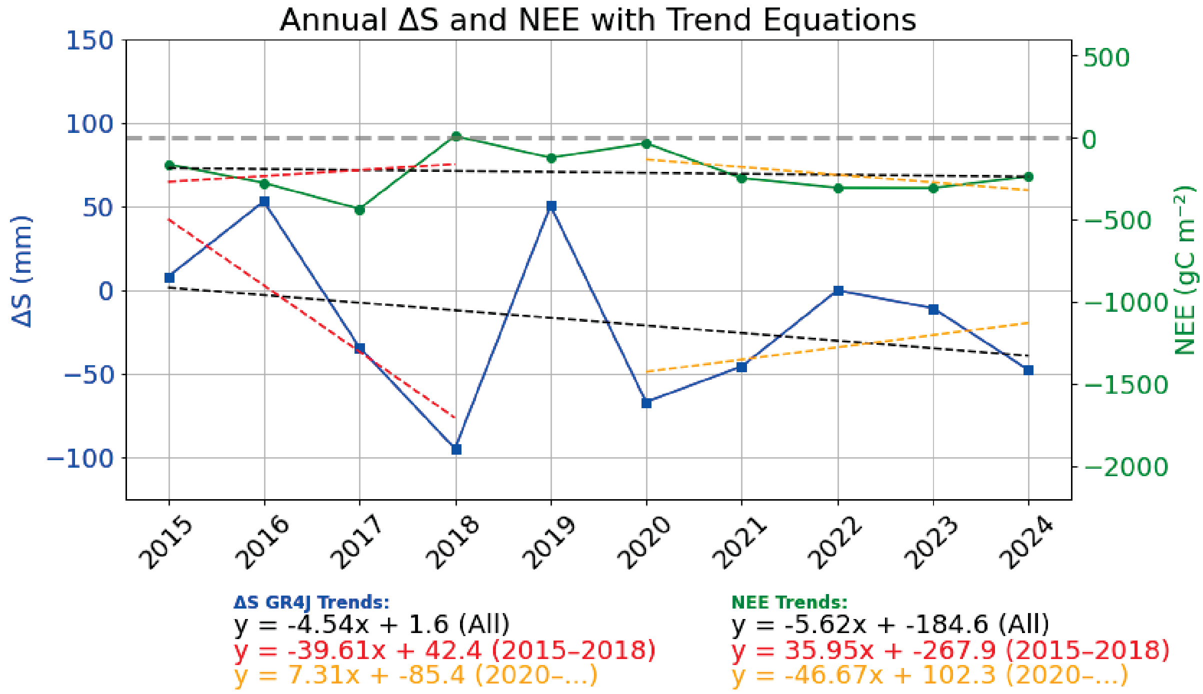

Figure 5.10: Interannual trends of Water Storage (ΔS) and Carbon Uptake (NEE) from 2015 to 2024. The blue line represents the annual water balance (left axis), and the green line represents the annual integrated NEE (right axis). Dashed lines indicate linear trends for the drying period (2015–2018, red) and the recovery period (2020–2024, orange), highlighting the correlation between water availability and carbon sequestration efficiency.

Chapter 6

Discussion

In this chapter, we critically interpret the outcomes of the study in the broader context of current scientific knowledge. The discussion is organized around three core contributions: (1) the demonstrated shift in hydrological modeling enabled by hybrid LSTM–GR4J architectures; (2) advances in the physical interpretability of deep learning models through diagnostic probes; and (3) a mechanistic understanding of carbon–water coupling, with emphasis on ecosystem resilience to extreme events and inferred causal interactions.

The hydrological evaluation in the Reola catchment shows that combining conceptual structure with deep learning substantially improves simulation skill. The hybrid LSTM–GR4J model outperformed both the standalone LSTM (NSE = 0.827) and the GR4J model (NSE = 0.503), achieving an NSE of 0.887. These results support an emerging paradigm in hydrology: process-based and data-driven approaches need not be viewed as competing frameworks, but can instead function synergistically.

As shown in Table 5.1, the hybrid model capitalized on the complementary strengths of each component. GR4J provided mass-balance constraints and snow dynamics (through the Cemaneige module), while the LSTM captured the nonlinear residual structure that the conceptual model could not represent (Kratzert et al., 2018). The resulting KGE of 0.890 reflects coherent improvements across correlation, bias, and variability.

Seasonal analyses (Figure 5.1) reveal distinct behavioral contrasts between the standalone models: GR4J underestimates peak flows during saturated periods, while the LSTM displays stronger reactivity. The hybrid model reconciles these tendencies, demonstrating that neural networks conditioned on hydrological state variables such as $S(t)$ and $G(t)$ can encode process nuances that neither model extracts in isolation.

The regionalization to the ungauged Kalli catchment highlights the challenges of transferring models between basins with differing physiographic characteristics. The divergence between the LSTM's flashy response and the more storage-driven behavior of GR4J in Kalli reflects uncertainties associated with the basin's greater proportion of peatlands and drainage ditches. Nevertheless, the consistency between regionalized LSTM simulations and local precipitation patterns suggests that deep learning models can generalize effectively when climatic regimes are shared across basins (Arsenault et al., 2023; Kratzert et al., 2019b).

A major obstacle in the adoption of AI in environmental sciences is the perceived black-box nature of deep learning models. Our diagnostic probe approach addressed this by validating the physical interpretability of the LSTM's internal states. The Support Vector Regression (SVR) probe successfully reconstructed soil moisture dynamics ($r > 0.9$ for intermediate layers) using only the LSTM's cell states—despite the network never being explicitly trained on soil moisture data. This provides empirical support for the hypothesis proposed by Lees et al. (2022) that LSTM states encode physically meaningful hydrological information.

High correlations with ERA5 (SWVL2) indicate that the LSTM did not simply fit a statistical curve to streamflow. Instead, the network learned an implicit representation of terrestrial water storage consistent with the requirements of the water balance equation. This confirms that LSTM internal states can serve as reliable proxies for hydrological storage variables.

The joint analysis of water balance (ΔS) and Net Ecosystem Exchange (NEE) provided insights into the resilience of the hemiboreal forest, with particular emphasis on the 2018 heatwave. The coupling between validated water balance and carbon fluxes revealed a clear tipping point. As shown in Figure 5.9, the synchronous divergence near DOY 150—marked by a sharp decline in ΔS and stagnation of NEE—indicates a physiological shift from energy-limited to water-limited photosynthesis.

A key finding of this study is the ecological hysteresis—or legacy effect—identified in the interannual trends (Figure 5.10). Despite a return to normal precipitation levels in 2019, carbon sequestration did not fully recover until 2020. This V-shaped recovery suggests that the 2018 drought induced persistent physiological damage—such as xylem cavitation, root mortality, or depletion of non-structural carbohydrates—that required multiple growing seasons to repair. These results reinforce the growing consensus that the *frequency* of extreme climatic events may be as consequential as their intensity, as recurrent droughts can inhibit recovery and push hemiboreal forests beyond critical resilience thresholds.

Despite the contributions of this study, several limitations should be acknowledged. (1) **Regionalization uncertainty:** The model transfer from Reola to Kalli assumes hydrological similarity. The greater peatland extent in Kalli may lead LSTM models trained on mineral soils to underestimate baseflow retention. (2) **Probe calibration:** The SVR probe depends on reference data (ERA5/SMAP), and its accuracy is bounded by the reliability of these products. (3) **Data length:** Although the 10-year record captures the 2018 extreme event, longer time series would be required to disentangle decadal climate trends from interannual variability with higher statistical confidence.

6.1 Conclusion

This dissertation delivered an integrated assessment of coupled water–carbon dynamics in a hemiboreal forest in Järvselja, Estonia, by combining a conceptual hydrological model (GR4J–CemaNeige), a data-driven recurrent neural network (LSTM), and eddy-covariance observations of carbon fluxes. Combining process-based and machine-learning approaches allowed evaluation of predictive performance and investigation of whether data-driven models develop physically meaningful internal representations (e.g., soil moisture dynamics). The framework also enabled quantifying ecosystem responses to climatic extremes across daily to annual time scales.

While the LSTM and the hybrid model achieved high predictive skill ($NSE > 0.80$), the conceptual GR4J provided a baseline performance ($NSE = 0.503$). The LSTM provided modest but consistent improvements in several objective metrics (higher KGE, lower RMSE and MAE, and smaller bias), indicating its capacity to represent temporal dependencies and nonlinear relationships that complement the parsimonious structure of the conceptual model. When regionalized to the ungauged Kalli basin, the LSTM reproduced seasonal streamflow patterns more similar to Reola observations, whereas GR4J preserved internal hydrological consistency—its storage components and routing behavior remained interpretable and coherent with water-balance expectations.

Applying a diagnostic probe based on Support Vector Regression (SVR) to stored LSTM cell states demonstrated that the LSTM internal representations encode information that correlates positively with independent soil moisture products (ERA5 layers and SMAP) and with *in-situ* water-level observations. Correlations were moderate to high (best for the ERA5 7–28 cm layer and the SMAP surface product), indicating that the network implicitly learns hydrologically relevant features while optimized for discharge prediction. However, the probe revealed systematic magnitude differences (bias and absolute errors) between probe outputs and physical measurements, implying that LSTM states capture relative dynamics and timing more reliably than absolute physical values. Therefore, probes constitute a valuable interpretability tool but require careful calibration and independent validation.

The joint analysis of catchment water balance ($\Delta S = P - ET - Q$) and Net Ecosystem Exchange (NEE) revealed a clear coupling between terrestrial water storage and carbon fluxes: reductions in storage coincided with decreased GPP and shifts of NEE toward neutrality or net CO_2 emission. This coupling was evident at monthly and annual aggregations and became most pronounced during extreme events. The 2018 heatwave exemplified this sensitivity: elevated temperatures combined with sustained water deficit produced a marked reduction in GPP, anomalous Water Use Efficiency (WUE) responses, and a transient collapse of the net carbon sink function. These results identify soil moisture and catchment storage dynamics as primary modulators of ecosystem resilience to heat and drought in hemiboreal forests.

Methodologically, this study demonstrates the complementarity of conceptual hydrological models and data-driven LSTM models in catchments with heterogeneous instrumentation. The conceptual model provides physically interpretable stores and flux partitioning, while the LSTM improves predictive accuracy and captures complex temporal patterns. The probe workflow (LSTM states → SVR → physical target) offers a pragmatic route to open black-box models to process-level inspection. Nonetheless, the findings also point to opportunities for methodological refinement—specifically, imposing physical constraints or hybrid architectures to reduce magnitude biases and enhance generalization.

Key limitations include the relatively short observational records available for robust deep-learning generalization, streamflow observations limited to Reola (necessitating regionalization for Kalli), and uncertainties introduced by gap-filling and by remote-sensing/reanalysis products (ERA5/SMAP). The probe is supervised and depends on the chosen regressor and target product; different probe designs and data sources may yield different associations. Finally, the linear regression analyses performed here provide a first-order characterization of water–carbon coupling but do not fully resolve causal, nonlinear, or confounding influences (e.g., VPD, diffuse radiation, nutrient status, stand structure).

To consolidate and extend the present findings, future work should: (1) extend temporal coverage and spatial replication (additional catchments and longer records) to strengthen regionalization and trend detection; (2) incorporate additional meteorological and physiological drivers (VPD, diffuse radiation, phenology indices) and quantify their roles in carbon–water interactions; (3) develop and evaluate hybrid model frameworks—such as physics-informed neural networks, constrained LSTMs, or modular hybrid architectures—that combine physical consistency with machine-learning flexibility to reduce magnitude biases in internal-state probes; (4) systematically benchmark probe variants (linear, kernelized, neural probes) and assess robustness through cross-basin and cross-period validation.

In summary, this dissertation advances both the mechanistic understanding of water–carbon coupling in hemiboreal forests and the methodological toolkit for their study. It demonstrates that maintaining terrestrial water availability is critical for sustaining the carbon-sink function of these forests and that integrated modeling—combining conceptual process models, interpretable machine learning, and flux observations—provides a robust pathway to quantify ecosystem sensitivity to extreme climatic events. Given the projected increase in the frequency and intensity of heat and drought events, further development of hybrid, physically constrained data-driven methods and expanded monitoring are essential for reliable assessment and management of forest carbon and water services.

Bibliography

Simone Massulini Acosta. Aplicação de redes neurais artificiais e regressão por vetores de suporte na modelagem da fração de produtos não conformes de um processo produtivo. *Universidade Federal de Campina Grande*, 2019.

João M. Andrade, Alfredo Ribeiro Neto, Rodolfo L.B. Nóbrega, Miguel A. Rico-Ramirez, and Suzana M.G.L. Montenegro. Efficiency of global precipitation datasets in tropical and subtropical catchments revealed by large sampling hydrological modelling. *Journal of Hydrology*, 633:131016, 2024. ISSN 0022-1694. doi: https://doi.org/10.1016/j.jhydrol.2024.131016. URL `https://www.sciencedirect.com/science/article/pii/S0022169424004116`.

Richard Arsenault, Jean-Luc Martel, Frédéric Brunet, François Brissette, and Juliane Mai. Continuous streamflow prediction in ungauged basins: long short-term memory neural networks clearly outperform traditional hydrological models. *Hydrology and Earth System Sciences*, 27(1):139–157, 2023.

Vladan Babovic. Introducing knowledge into learning based on genetic programming. *Journal of Hydroinformatics*, 11(3-4):181–193, 2009.

Ana Bastos, Zheng Fu, Philippe Ciais, Pierre Friedlingstein, Stephen Sitch, Julia Pongratz, Ulrich Weber, Markus Reichstein, Peter Anthoni, Almut Arneth, et al. Impacts of extreme summers on european ecosystems: a comparative analysis of 2003, 2010 and 2018. *Philosophical Transactions of the Royal Society B*, 375(1810):20190507, 2020.

Wilfried Brutsaert. *Hydrology: An Introduction*. Cambridge University Press, 2005.

George Burba. Principles of eddy covariance technique. In *Eddy Covariance Method for Scientific, Industrial, Agricultural, and Regulatory Applications: A Field Book on Measuring Ecosystem Gas Exchange and Areal Emission Rates*, pages 21–45. LI-COR Biosciences, Lincoln, NE, 2013. ISBN 9780615800790.

Angélica Luciana Barros de Campos. Estudo de um modelo de otimização dos custos de energia elétrica do bombeamento em sistema de abastecimento de água. Dissertação de mestrado, Universidade Federal de Pernambuco, Recife, Brasil, 2017.

Elia Cantoni, Yves Tramblay, Stefania Grimaldi, Peter Salamon, Hamouda Dakhlaoui, Alain Dezetter, and Vera Thiemig. Hydrological performance of the era5 reanalysis for flood modeling in tunisia with the lisflood and gr4j models. *Journal of Hydrology: Regional Studies*, 42:101169, 2022. ISSN 2214-5818. doi: https://doi.org/10.1016/j.ejrh.2022.101169. URL `https://www.sciencedirect.com/science/article/pii/S2214581822001823`.

F SIII Chapin, George M Woodwell, James T Randerson, Edward B Rastetter, Gary M Lovett, Dennis D Baldocchi, Deborah A Clark, Mark E Harmon, David S Schimel, R Valentini, et al. Reconciling carbon-cycle concepts, terminology, and methods. *Ecosystems*, 9:1041–1050, 2006.

Hendrik Davi, E Dufrêne, C Francois, Guerric Le Maire, Denis Loustau, Alexandre Bosc, Serge Rambal, André Granier, and E Moors. Sensitivity of water and carbon fluxes to climate changes from 1960 to 2100 in european forest ecosystems. *Agricultural and Forest Meteorology*, 141 (1):35–56, 2006.

DG AGRI. Commission recommendations for estonia's cap strategic plan. Staff working document SWD/2020/375 final, European Commission, December 2020. URL `https://eur-lex.europa.eu/legal-content/EN/TXT/?uri=SWD%3A2020%3A375%3AFIN`. Forwarded to the Council and the European Parliament on 18 December 2020.

Xianming Dou and Yongguo Yang. Modeling and predicting carbon and water fluxes using data-driven techniques in a forest ecosystem. *Forests*, 8(12):498, 2017.

Xianming Dou, Yongguo Yang, and Jinhui Luo. Estimating forest carbon fluxes using machine learning techniques based on eddy covariance measurements. *Sustainability*, 10(1):203, 2018.

Estonian Environment Agency. Climate normals - precipitation. `https://www.ilmateenistus.ee/kliima/kliimanormid/sademed/?lang=en`, 2025. Accessed: 2025-06-19.

Estonian Ministry of Climate. Forestry. `https://kliimaministeerium.ee/en/biodiversity-environmental-protection/forestry`, 2024. Accessed: 10 June 2025.

Estonian Ministry of Environment. Estonian ministry of environment - forestry. `https://web.archive.org/web/20130401064414/http://www.envir.ee/67248`, 2013. Archived on April 1, 2013; Accessed: 10 June 2025.

European Commission. Statistical factsheet: Estonia, June 2020. URL `https://agriculture.ec.europa.eu/cap-my-country/performance-agricultural-policy/agriculture-country/eu-country-factsheets_en`. Page 6. Accessed: 12 May 2025.

European Union. Estonia – eu member country, 2025. URL `https://european-union.europa.eu/principles-countries-history/eu-countries/estonia_en`. Accessed: 12 May 2025.

Martin Evans. Water and carbon cycling: New a level subject content overview, 2016.

Ekaterina Ezhova, Topi Laanti, Anna Lintunen, Pasi Kolari, Tuomo Nieminen, Ivan Mammarella, Keijo Heljanko, and Markku Kulmala. Explainable machine learning for modeling of net ecosystem exchange in boreal forests. *Biogeosciences*, 22(1):257–288, 2025.

FAO. Global forest resources assessment 2020 – estonia country report, 2020. URL `https://fra-platform.herokuapp.com/assessments/fra/2020/EST/home/overview`. Accessed: 12 May 2025.

Jonathan M Frame and Kratzert. Deep learning rainfall–runoff predictions of extreme events. *Hydrology and Earth System Sciences*, 26(13):3377–3392, 2022.

P. Friedlingstein. Global carbon budget 2023. *Earth System Science Data*, 15(12):5301–5369, 2023. doi: 10.5194/essd-15-5301-2023. URL `https://essd.copernicus.org/articles/15/5301/2023/`.

Fatemeh Ghobadi and Doosun Kang. Application of machine learning in water resources management: a systematic literature review. *Water*, 15(4):620, 2023.

Ruikun Gou, Nina Buchmann, Jinshu Chi, Yunpeng Luo, Lidong Mo, Ankit Shekhar, Iris Feigenwinter, Lukas Hörtnagl, Weizhi Lu, Xiaowei Cui, Yuchen Meng, Shanshan Song, Guangxuan Lin, Yuechao Chen, Jie Liang, Jiemin Guo, Haijun Peng, and Guanghui Lin. Temporal variations of carbon and water fluxes in a subtropical mangrove forest: Insights from a decade-long eddy covariance measurement. *Agricultural and Forest Meteorology*, 343:109764, 2023. ISSN 0168-1923. doi: https://doi.org/10.1016/j.agrformet.2023.109764. URL `https://www.sciencedirect.com/science/article/pii/S0168192323004549`.

Alex Graves and Jürgen Schmidhuber. Framewise phoneme classification with bidirectional lstm and other neural network architectures. *Neural Networks*, 18(5):602–610, 2005. ISSN 0893-6080. doi: https://doi.org/10.1016/j.neunet.2005.06.042. URL `https://www.sciencedirect.com/science/article/pii/S0893608005001206`. IJCNN 2005.

B. Gschwind, L. Wald, P. Blanc, M. Lefèvre, M. Schroedter-Homscheidt, and A. Arola. Improving the McClear model estimating the downwelling solar radiation at ground level in cloud free conditions – McClear-V3. *Meteorologische Zeitschrift / Contributions to Atmospheric Science*, 28(2):147–163, 2019. doi: 10.1127/metz/2019/0946. URL `https://www.schweizerbart.de/papers/metz/detail/28/90593/Improving_the_McClear_model_estimating_the_downwelling_solar_radiation_at_ground_level_in_cloud_free_conditions_McClear_v3`.

Lei Gu. How well do the multi-satellite and atmospheric reanalysis products perform in hydrological modelling. *Journal of Hydrology*, 617:128920, 2023. ISSN 0022-1694. doi: https://doi.org/10.1016/j.jhydrol.2022.128920. URL `https://www.sciencedirect.com/science/article/pii/S0022169422014901`.

Hoshin V Gupta, Hannes Kling, Koray K Yilmaz, and Guillermo F Martinez. Decomposition of the mean squared error and nash–sutcliffe efficiency performance criteria: Implications for improving hydrological modelling. *Journal of Hydrology*, 377(1-2):80–91, 2009.

Pertti Hari, Eero Nikinmaa, Toivo Pohja, Erkki Siivola, Jaana Bäck, Timo Vesala, and Markku Kulmala. *Station for Measuring Ecosystem-Atmosphere Relations: SMEAR*, pages 471–487. Springer Netherlands, Dordrecht, 2013. ISBN 978-94-007-5603-8. doi: 10.1007/978-94-007-5603-8_9. URL `https://doi.org/10.1007/978-94-007-5603-8_9`.

Matthew N Hayek, Marcos Longo, Jin Wu, Marielle N Smith, Natalia Restrepo-Coupe, Raphael Tapajós, Rodrigo Da Silva, David R Fitzjarrald, Plinio B Camargo, Lucy R Hutyra, et al. Carbon exchange in an amazon forest: from hours to years. *Biogeosciences*, 15(15):4833–4848, 2018.

H. Hersbach. Complete ERA5 from 1940: Fifth generation of ECMWF atmospheric reanalyses of the global climate, 2017. URL `https://doi.org/10.24381/cds.143582cf`. Accessed on 06-05-2025.

H. Hersbach, B. Bell, P. Berrisford, G. Biavati, A. Horányi, J. Muñoz Sabater, J. Nicolas, C. Peubey, R. Radu, I. Rozum, D. Schepers, A. Simmons, C. Soci, D. Dee, and J-N. Thépaut. ERA5 hourly data on single levels from 1940 to present. Copernicus Climate Change Service (C3S) Climate Data Store (CDS), 2023. Accessed on 05-05-2024.

Sepp Hochreiter and Jürgen Schmidhuber. Long short-term memory. *Neural computation*, 9(8): 1735–1780, 1997.

Rob J. Hyndman and Anne B. Koehler. Another look at measures of forecast accuracy. *International Journal of Forecasting*, 22(4):679–688, 2006. ISSN 0169-2070. doi: https://doi.org/10.1016/j.ijforecast.2006.03.001. URL `https://www.sciencedirect.com/science/article/pii/S0169207006000239`.

Shigehiro Ishizuka, Tadashi Sakata, Satoshi Sawata, Shigeto Ikeda, Chisato Takenaka, Nobuaki Tamai, Hisao Sakai, Takanori Shimizu, Kensaku Kan-Na, Shinichi Onodera, et al. High potential for increase in co _{2} flux from forest soil surface due to global warming in cooler areas of japan. *Annals of forest science*, 63(5):537–546, 2006.

Nischal Karki. Comparative performance of regionalization methods for model parameterization in ungauged himalayan watersheds. *Journal of Hydrology: Regional Studies*, 47:101359, 2023. ISSN 2214-5818. doi: https://doi.org/10.1016/j.ejrh.2023.101359. URL `https://www.sciencedirect.com/science/article/pii/S2214581823000460`.

Andrej Karpathy. The unreasonable effectiveness of recurrent neural networks, may 2015. URL `https://karpathy.github.io/2015/05/21/rnn-effectiveness/`.

Mohammad Kazemi Garajeh, Fatemeh Haji, Mahsa Tohidfar, Amin Sadeqi, Reyhaneh Ahmadi, and Narges Kariminejad. Spatiotemporal monitoring of climate change impacts on water resources using an integrated approach of remote sensing and google earth engine. *Scientific reports*, 14(1):5469, 2024.

Reza Khanbilvardi, Tarendra Lakhankar, Nir Krakauer, Rouzbeh Nazari, and Al Powell. Remote sensing data and information for hydrological monitoring and modeling. *Handbook of Engineering Hydrology: Modeling, Climate Change, and Variability*, pages 501–516, 2014.

Ricardo Alfredo Kluge, Jaqueline V Tezotto-Uliana, and Paula PM da Silva. Aspectos fisiológicos e ambientais da fotossíntese. *Revista virtual de química*, 7(1):56–73, 2015.

Ch Körner. Leaf diffusive conductances in the major vegetation types of the globe. In *Ecophysiology of photosynthesis*, pages 463–490. Springer, 1995.

A. Krasnova, Ü. Mander, S.M. Noe, V. Uri, D. Krasnov, and K. Soosaar. Hemiboreal forests' co2 fluxes response to the european 2018 heatwave. *Agricultural and Forest Meteorology*, 323:109042, 2022. ISSN 0168-1923. doi: https://doi.org/10.1016/j.agrformet.2022.109042. URL `https://www.sciencedirect.com/science/article/pii/S0168192322002313`.

Alisa Krasnova. Carbon exchange in a hemiboreal mixed forest in relation to tree species composition. *Agricultural and Forest Meteorology*, 275:11–23, 2019. ISSN 0168-1923. doi: https://doi.org/10.1016/j.agrformet.2019.05.007. URL `https://www.sciencedirect.com/science/article/pii/S0168192319301789`.

Frederik Kratzert, Daniel Klotz, Claire Brenner, Karsten Schulz, and Mathew Herrnegger. Rainfall–runoff modelling using long short-term memory (lstm) networks. *Hydrology and Earth System Sciences*, 22(11):6005–6022, 2018.

Frederik Kratzert, Daniel Klotz, Mathew Herrnegger, Alden K Sampson, Sepp Hochreiter, and Grey S Nearing. Toward improved predictions in ungauged basins: Exploiting the power of machine learning. *Water Resources Research*, 55(12):11344–11354, 2019a.

Frederik Kratzert, Daniel Klotz, Guy Shalev, Günter Klambauer, Sepp Hochreiter, and Grey Nearing. Towards learning universal, regional, and local hydrological behaviors via machine learning applied to large-sample datasets. *Hydrology and Earth System Sciences*, 23(12): 5089–5110, 2019b.

L. A. Kuana, A. S. Almeida, E. G. F. Mercuri, and S. M. Noe. Regionalization of gr4j model parameters for river flow prediction in paraná, brazil. *Hydrology and Earth System Sciences*, 28(14):3367–3390, 2024. doi: 10.5194/hess-28-3367-2024. URL `https://hess.copernicus.org/articles/28/3367/2024/`.

Gitta Lasslop, Markus Reichstein, Dario Papale, Andrew D Richardson, Almut Arneth, Alan Barr, Paul Stoy, and Georg Wohlfahrt. Separation of net ecosystem exchange into assimilation and respiration using a light response curve approach: critical issues and global evaluation. *Global change biology*, 16(1):187–208, 2010.

T. Lees, S. Reece, F. Kratzert, D. Klotz, M. Gauch, J. De Bruijn, R. Kumar Sahu, P. Greve, L. Slater, and S. J. Dadson. Hydrological concept formation inside long short-term memory (lstm) networks. *Hydrology and Earth System Sciences*, 26(12):3079–3101, 2022. doi: 10.5194/hess-26-3079-2022. URL `https://hess.copernicus.org/articles/26/3079/2022/`.

Anders Lindroth, Jutta Holst, Michal Heliasz, Patrik Vestin, Fredrik Lagergren, Tobias Biermann, Zhanzhang Cai, and Meelis Mölder. Effects of low thinning on carbon dioxide fluxes in a mixed hemiboreal forest. *Agricultural and Forest Meteorology*, 262:59–70, 2018.

John Lloyd and JA Taylor. On the temperature dependence of soil respiration. *Functional ecology*, pages 315–323, 1994.

Meinshausen. The shared socio-economic pathway (ssp) greenhouse gas concentrations and their extensions to 2500. *Geoscientific Model Development*, 13(8):3571–3605, 2020. doi: 10.5194/gmd-13-3571-2020. URL `https://gmd.copernicus.org/articles/13/3571/2020/`.

Keila R Mendes, Suany Campos, Lindenberg L da Silva, Pedro R Mutti, Rosaria R Ferreira, Salomão S Medeiros, Aldrin M Perez-Marin, Thiago V Marques, Tarsila M Ramos, Mariana M de Lima Vieira, et al. Seasonal variation in net ecosystem co2 exchange of a brazilian seasonally dry tropical forest. *Scientific Reports*, 10(1):9454, 2020.

Emílio Graciliano Ferreira Mercuri, Toomas Tamm, and Steffen Manfred Noe. Water and carbon balances in a hemi-boreal forest. *Forestry Studies*, 78(1):72–90, 2023.

Babak Mohammadi. A review on the applications of machine learning for runoff modeling. *Sustainable Water Resources Management*, 7(6):98, 2021.

Shashank Mohan, Brajesh Kumar, and A Pouyan Nejadhashemi. Integration of machine learning and remote sensing for water quality monitoring and prediction: A review. *Sustainability*, 17 (3):998, 2025.

J E Nash and J V Sutcliffe. River flow forecasting through conceptual models part i–a discussion of principles. *Journal of Hydrology*, 10(3):282–290, 1970.

Saida Nemri and Christophe Kinnard. Comparing calibration strategies of a conceptual snow hydrology model and their impact on model performance and parameter identifiability. *Journal of Hydrology*, 582:124474, 2020. ISSN 0022-1694. doi: https://doi.org/10.1016/j.jhydrol.2019.124474. URL `https://www.sciencedirect.com/science/article/pii/S0022169419312090`.

NOAA . No sign of greenhouse gases increases slowing in 2023,noaa global monitoring laboratory. `https://research.noaa.gov/no-sign-of-greenhouse-gases-increases-slowing-in-2023/`, 2024. Accessed: 2025-05-19.

Steffen M Noe and Niinemets. Smear estonia: Perspectives of a large-scale forest ecosystem–atmosphere research infrastructure. *Metsanduslikud uurimused*, 63(1):56–84, 2015.

P. E. O'Neill, S. Chan, E. G. Njoku, T. Jackson, R. Bindlish, J. Chaubell, and A. Colliander. SMAP Enhanced L2 Radiometer Half-Orbit 9 km EASE-Grid Soil Moisture (SPL2SMP_E, Version 6), 2023. URL `https://doi.org/10.5067/BN36FXOMMC4C`. Date Accessed 06-10-2025.

X. Pan, W. Helgason, A. Ireson, and H. Wheater. Field-scale water balance closure in seasonally frozen conditions. *Hydrology and Earth System Sciences*, 21(11):5401–5413, 2017. doi: 10.5194/hess-21-5401-2017. URL `https://hess.copernicus.org/articles/21/5401/2017/`.

Karl Pearson. Mathematical contributions to the theory of evolution.–iii. regression, heredity, and panmixia. *Philosophical Transactions of the Royal Society of London. A*, 187:253–318, 1896.

Charles Perrin, Claude Michel, and Vazken Andréassian. Improvement of a parsimonious model for streamflow simulation. *Journal of Hydrology*, 279(1):275–289, 2003. ISSN 0022-1694. doi: https://doi.org/10.1016/S0022-1694(03)00225-7. URL `https://www.sciencedirect.com/science/article/pii/S0022169403002257`.

Wouter Peters, Ana Bastos, Philippe Ciais, and Alex Vermeulen. A historical, geographical and ecological perspective on the 2018 european summer drought, 2020.

Kim Pilegaard and Andreas Ibrom. Net carbon ecosystem exchange during 24 years in the sorø beech forest–relations to phenology and climate. *Tellus B: Chemical and Physical Meteorology*, 72(1):1–17, 2020.

Karena Quiroz Jiménez and Walter Collischonn. Método de combinação de dados de precipitação estimados por satélite e medidos em pluviômetros para a modelagem hidrológica. *Rbrh: revista brasileira de recursos hídricos. Porto Alegre, RS. Vol. 20, n. 1 (jan./mar. 2015), p. 202-217*, 2015.

Maziar Raissi, Paris Perdikaris, Nazanin Ahmadi, and George Em Karniadakis. Physics-informed neural networks and extensions. *arXiv preprint arXiv:2408.16806*, 2024.

Saman Razavi, David M Hannah, Amin Elshorbagy, Sujay Kumar, Lucy Marshall, Dimitri P Solomatine, Amin Dezfuli, Mojtaba Sadegh, and James Famiglietti. Coevolution of machine learning and process-based modelling to revolutionize earth and environmental sciences: A perspective. *Hydrological Processes*, 36(6):e14596, 2022.

David E. Reichle. Chapter 8 - energy flow in ecosystems. In David E. Reichle, editor, *The Global Carbon Cycle and Climate Change*, pages 119–156. Elsevier, 2020. ISBN 978-0-12-820244-9. doi: https://doi.org/10.1016/B978-0-12-820244-9.00008-1. URL `https://www.sciencedirect.com/science/article/pii/B9780128202449000081`.

Markus Reichstein, Eva Falge, Dennis Baldocchi, Dario Papale, Marc Aubinet, Paul Berbigier, Christian Bernhofer, Nina Buchmann, Tagir Gilmanov, Andre Granier, et al. On the separation of net ecosystem exchange into assimilation and ecosystem respiration: review and improved algorithm. *Global change biology*, 11(9):1424–1439, 2005.

Behmard Sabzipour, Richard Arsenault, Magali Troin, Jean-Luc Martel, François Brissette, Frédéric Brunet, and Juliane Mai. Comparing a long short-term memory (lstm) neural network with a physically-based hydrological model for streamflow forecasting over a canadian catchment. *Journal of Hydrology*, 627:130380, 2023. ISSN 0022-1694. doi: https://doi.org/10.1016/j.jhydrol.2023.130380. URL `https://www.sciencedirect.com/science/article/pii/S0022169423013227`.

Mohammad Safeeq, Ryan R Bart, Norman F Pelak, Chandan K Singh, David N Dralle, Peter Hartsough, and Joseph W Wagenbrenner. How realistic are water-balance closure assumptions? a demonstration from the southern sierra critical zone observatory and kings river experimental watersheds. *Hydrological Processes*, 35(5):e14199, 2021.

Asish Saha and Subodh Chandra Pal. Application of machine learning and emerging remote sensing techniques in hydrology: A state-of-the-art review and current research trends. *Journal of Hydrology*, 632:130907, 2024.

Bibhuti Bhusan Sahoo, Ramakar Jha, Anshuman Singh, and Deepak Kumar. Long short-term memory (lstm) recurrent neural network for low-flow hydrological time series forecasting. *Acta Geophysica*, 67(5):1471–1481, 2019.

SMEAR Estonia. SMEAR Estonia Data Portal. `https://smear.emu.ee/index.php`, 2025. Accessed: 2025-05-01.

John S Sperry, Martin D Venturas, Henry N Todd, Anna T Trugman, William RL Anderegg, Yujie Wang, and Xiaonan Tai. The impact of rising co2 and acclimation on the response of us forests to global warming. *Proceedings of the National Academy of Sciences*, 116(51): 25734–25744, 2019.

Stephen M Stigler. *The History of Statistics: The Measurement of Uncertainty Before 1900*. Harvard University Press, 1986.

J Teng, NJ Potter, FHS Chiew, L Zhang, B Wang, J Vaze, and JP Evans. How does bias correction of regional climate model precipitation affect modelled runoff? *Hydrology and Earth System Sciences*, 19(2):711–728, 2015.

Bryan A Tolson and Christine A Shoemaker. Dynamically dimensioned search algorithm for computationally efficient watershed model calibration. *Water Resources Research*, 43(1), 2007.

Alexis Valéry. *Modélisation précipitations-débit sous influence nivale: Élaboration d'un module neige et évaluation sur 380 bassins versants*. Thèse de doctorat, AgroParisTech, Paris, France, 2010.

Vladimir Vapnik. *Statistical Learning Theory now plays a more active role: after the general analysis of learning processes, the research in the area of synthesis of optimal algorithms was started. These studies, however, do not belong to history yet. They are a subject of today's research activities.* PhD thesis, These studies, however, do not belong to history yet. They are a subject of . . . , 1998.

Kok Poh Wai, Min Yan Chia, Chai Hoon Koo, Yuk Feng Huang, and Woon Chan Chong. Applications of deep learning in water quality management: A state-of-the-art review. *Journal of Hydrology*, 613:128332, 2022. ISSN 0022-1694. doi: https://doi.org/10.1016/j.jhydrol.2022.128332. URL `https://www.sciencedirect.com/science/article/pii/S0022169422009040`.

R. H. Waring and S. W. Running. *Forest Ecosystems: Analysis at Multiple Scales*. Academic Press, San Diego, CA, USA, 1998.

Dayal Buddika Wijayarathne and Paulin Coulibaly. Identification of hydrological models for operational flood forecasting in st. john's, newfoundland, canada. *Journal of Hydrology: Regional Studies*, 27:100646, 2020. ISSN 2214-5818. doi: https://doi.org/10.1016/j.ejrh.2019.100646. URL `https://www.sciencedirect.com/science/article/pii/S2214581819300679`.

Andrew W Wood, Lai R Leung, Venkataramana Sridhar, and Dennis P Lettenmaier. Hydrologic implications of dynamical and statistical approaches to downscaling climate model outputs. *Climatic change*, 62(1):189–216, 2004.

T. Wutzler, A. Lucas-Moffat, M. Migliavacca, J. Knauer, K. Sickel, L. Šigut, O. Menzer, and M. Reichstein. Basic and extensible post-processing of eddy covariance flux data with reddyproc. *Biogeosciences*, 15(16):5015–5030, 2018. doi: 10.5194/bg-15-5015-2018. URL `https://bg.copernicus.org/articles/15/5015/2018/`.

Tianfang Xu and Feng Liang. Machine learning for hydrologic sciences: An introductory overview. *Wiley Interdisciplinary Reviews: Water*, 8(5):e1533, 2021.

Jianfeng Zhang, Yan Zhu, Xiaoping Zhang, Ming Ye, and Jinzhong Yang. Developing a long short-term memory (lstm) based model for predicting water table depth in agricultural areas. *Journal of Hydrology*, 561:918–929, 2018. ISSN 0022-1694. doi: https://doi.org/10.1016/j.jhydrol.2018.04.065. URL `https://www.sciencedirect.com/science/article/pii/S0022169418303184`.

Zhi-Hua Zhou. *Machine learning*. Springer nature, 2021.